Geophysical Journal International

Geophys. J. Int. (2022) **231,** 650–672
Advance Access publication 2022 June 9
GJI Geomagnetism, Rock Magnetism and Palaeomagnetism

https://doi.org/10.1093/gji/ggac212

A taxonomy of simulated geomagnetic jerks

Julien Aubert [1], Philip W. Livermore [2], Christopher C. Finlay,[3] Alexandre Fournier [1] and Nicolas Gillet[4]

[1] *Institut de physique du globe de Paris, CNRS, Université Paris Cité, F-*75005 *Paris, France. E-mail: aubert@ipgp.fr*
[2] *School of Earth and Environment, University of Leeds, Woodhouse, Leeds LS2 9JT, UK*
[3] *DTU Space, Technical University of Denmark, 2800 Kongens Lyngby, Copenhagen, Denmark*
[4] *Université Grenoble Alpes, Université Savoie Mont Blanc, CNRS, IRD, UGE, F-*38000 *Grenoble, France*

Accepted 2022 June 6. Received 2022 June 2; in original form 2022 February 8

SUMMARY

Geomagnetic jerks—abrupt changes in the acceleration of Earth's magnetic field that punctuate geomagnetic records— have been richly documented over the past decades by taking advantage of the complementary strengths of ground observatory and satellite measurements. It has recently been proposed that these events originate from the interplay and timescale separation between slow convection and rapid hydromagnetic wave propagation in Earth's outer core, with these latter waves playing a key role in the generation of jerk signals. To assess the generality of this explanation, here we analyse a catalogue of 14 events obtained during a 14 000-yr-long temporal sequence from a numerical geodynamo simulation that is the closest to date to Earth's core conditions regarding timescale separation. Events are classified according to their dynamic origin and the depth at which they are triggered in the outer core. The majority of jerk events are found to arise from intermittent local disruptions of the leading-order force balance between the pressure, Coriolis, buoyancy and Lorentz forces (the QG-MAC balance), that leads to an inertial compensation through the emission of rapid, non-axisymmetric, quasi-geostrophic Alfvén waves from the region where this force balance is disrupted. Jerk events of moderate strength arise from the arrival at low latitudes at the core surface of hydromagnetic wave packets emitted from convective plumes rooted at the inner core boundary. As in an earlier simulation, these account well for jerk features that have recently been documented by satellite and ground observations. The more realistic timescales in the simulation reported here allow further details to be distinguished, such as multiple temporal alternations of geomagnetic acceleration pulses at low latitudes, long-range synchronization of pulse foci in space and rapid longitudinal drift of these foci at the core surface. The strongest events in the catalogue arise from disruption of the leading-order force balance near or at the core surface, from the combined influence of the arrival of buoyancy plumes and magnetic field rearrangement. The hydromagnetic waves that are sent laterally and downwards generate signals that clearly illustrate the presence of nearly synchronous 'V-shaped' magnetic variation patterns over a wide portion of Earth's surface and also at mid to high latitudes, despite the source being confined to low latitudes at the core surface. Other well-known characteristics of strong geomagnetic jerks such as surges in the intensity of the secular variation and inflexions in the length-of-day variations are also reproduced in these events. Irrespectively of the event strength, our results support the hypothesis of a single physical root cause—the emission of magneto-inertial waves following a disruption of the QG-MAC balance—for jerks observed throughout the geomagnetic record.

Key words: Dynamo: theories and simulations; satellite magnetics; Rapid time variations.

1 INTRODUCTION

The Earth's magnetic field displays variability on a broad range of timescales, as a result of a wide separation between key temporal and spatial scales in the geodynamo magnetohydrodynamic process that sustains this field. At the shorter end of the timescale spectrum that is accessible from observations, geomagnetic jerks involve large and rapid changes in the geomagnetic acceleration, the second time

derivative of the geomagnetic field. By 'rapid', it is understood that these changes take place on a sub-annual to interannual timescale that is much shorter than the secular overturn time of Earth's core $\tau_U = D/U \approx 130$ yr, where $D = 2260$ km is the thickness of the outer core and $U = 17$ km yr^{-1} is a typical velocity for fluid flow at the surface of the core (e.g. Gillet *et al.* 2015; Aubert 2015; Bärenzung *et al.* 2018). By 'large', it is meant that the changes exceed the typical amplitude of accelerations observed over decadal and longer periods (e.g. Lesur *et al.* 2022).

Ground observatory measurements of the geomagnetic field offer a unique perspective on jerks because they offer long, highly detailed time-series at a fixed location in space. The first detection of a jerk event in 1969–1970 relied on an analysis of time-series of the first derivative of geomagnetic field components (the secular variation) at mid-latitude observatories of the Northern hemisphere (Courtillot *et al.* 1978; Malin *et al.* 1983). The classical method of jerk detection, used for instance for the best documented events of the twentieth century (1969, 1978 and 1991), relies on the identification of a 'V-shape', that is a sudden change in the slope of the secular variation time-series that separates two decadal intervals with linear behaviour, hence a step change in an otherwise approximately constant acceleration (e.g. Mandea *et al.* 2010). Perhaps the most initially intriguing feature of clear jerks observed during the observatory era (1969, 1978, 1991 again) is that they have been labelled as worldwide, that is occurring quasi-simultaneously at remote observatories over the land surface of the Earth (Le Mouël *et al.* 1982; Alexandrescu *et al.* 1996; De Michelis *et al.* 1998; Pinheiro *et al.* 2011). In their reappraisal of the V-shape detection method, Brown *et al.* (2013) however underlined a common problem faced by the community: like all other known methods, this contains an implicit expectation of a large step change in the geomagnetic acceleration, without a clear definition of a common threshold other than that required for this change to be observable above other contaminating magnetic field sources. Following on this, Brown *et al.* (2013) nevertheless showed that the observatory data of the 20th century suggests that jerk events may be far more numerous than the few original historical landmarks, and also sometimes closely clustered, with the best known historical events presenting the clearest signal and the best temporal isolation. However, even for these latter events, Brown *et al.* (2013) noted that a systematic detection does not occur at more than 30 per cent of observatories worldwide within a given year. This indicates that the simultaneity of signatures ascribed to observed jerk events is not perfect, with regional delays up to 2 yr being routine (Pinheiro *et al.* 2011), and that the events may in fact be less global than commonly thought. This is in agreement with analyses of 'V-shapes' in observatory data of the past 20 yr (Chulliat *et al.* 2010; Torta *et al.* 2015; Soloviev *et al.* 2017; Finlay *et al.* 2020), none of which have found evidence of global simultaneous events.

Spherical harmonic modelling of the geomagnetic acceleration changes during the best documented events has indicated that these originate inside the Earth (e.g. Malin & Hodder 1982; Le Huy *et al.* 1998). The global acceleration maps obtained in these works are suggestive of widespread patterns of simultaneous secular acceleration changes at Earth surface, although the resolution of these studies was limited by the coverage of Earth surface by ground observatories. The advent of global and continuous monitoring of the geomagnetic field by satellites after 1999 has removed this limitation, now giving access to two decades of global geomagnetic acceleration that can be imaged down to the core surface with a spatial resolution up to spherical harmonic degree 9 (down to 2300 km in lateral resolution, Lesur *et al.* 2010; Finlay *et al.* 2020). Local time sampling by polar orbiting satellites, and most notably the difficulties of separating internal and external geomagnetic signals currently limit the temporal resolution at which the acceleration can be retrieved down to about a year (e.g. Lesur *et al.* 2022). The respective temporal and spatial resolution advantages of observatory and satellite data are therefore best exploited when the two sources of data are used in conjunction, as has been done after 1999 in global field models such as the CHAOS series (most recently Finlay *et al.* 2020). The global, time-varying core surface acceleration maps provided by these models indicate that jerk events correspond to sequences of short-lived pulses in the secular acceleration that are often localized at low latitude and in narrow longitudinal bands, and that their polarity rapidly alternates in time (Chulliat *et al.* 2010). They have also highlighted a long-range azimuthal relation and synchronization of secular acceleration pulse foci at the core surface, and an apparent rapid azimuthal drift of these foci (Chulliat *et al.* 2015). The jerks observed using ground and satellite data over the past 20 yr therefore appear to be associated with coherent temporal sequences where the step change in secular acceleration alternates in sign at each new event (Le Huy *et al.* 1998; Chulliat *et al.* 2015; Finlay *et al.* 2016), as is for instance the case in 2003, 2007, 2011 and 2014. The earlier historical events observed using ground observatory data in 1969, 1979 and 1991 appear to share this property but apparently with a longer (decadal) recurrence time. We complete this overview of the observational picture by mentioning a few secondary characteristics that have been reported—the occurrence of surges in the energy of secular variation at Earth's surface in the vicinity of jerk times (e.g. Jackson & Finlay 2015) and a possible link between jerks and small inflexions in the time derivative of the length of the day (Holme & de Viron 2005, 2013; Duan & Huang 2020).

The phenomenology of geomagnetic jerks presented above is rather daunting, and many aspects remain unclear due to limitations in the observations and their interpretations. One may even wonder whether all the observed events can be ascribed to a common physical root cause. The phenomenology presented above may certainly have suffered from biases related to the type of data available at each event epoch, from local secular variation time-series enabling the isolation of 'V-shapes' to global, time-dependent maps revealing secular acceleration pulses. The physical modelling of core dynamics, and particularly new numerical simulations of the geodynamo able to reproduce geomagnetic jerks in conditions approaching those of the Earth's core (Aubert & Finlay 2019) thus presents a possibility to rationalize the taxonomy of jerks and in particular classify their physical causes; these goals motivate this study.

The key requirement to reproduce jerks in a dynamic model is to obtain a suitable separation between the secular overturn timescale τ_U, the interannual Alfvén timescale $\tau_A = \sqrt{\rho\mu}D/B$ and the daily planetary rotation timescale $\tau_\Omega = 1/\Omega$ (where ρ, μ are the fluid density and magnetic permeability, B is a typical magnetic field amplitude in the core and Ω is the rotation rate of the planet). The explanation proposed by Aubert & Finlay (2019) rests on the existence of rapid magneto-inertial waves that cause signals on timescales commensurate with τ_A (and hence much shorter than τ_U), that are additionally strongly constrained by the Coriolis force since $\tau_A \gg \tau_\Omega$. Here we wish to assess the generality of this explanation, first by investigating the recent simulation of Aubert & Gillet (2021, from hereafter AG21) that brings the separation between the key timescales τ_U, τ_A and τ_Ω closer to the target defined by Earth's core conditions (see Table 1), and second by analysing a larger number of simulated jerk events than the set presented in Aubert & Finlay

Table 1. Key timescales and their values for the 71p model and Earth's core. Estimates for Earth's core are obtained with the root-mean-squared velocity inside the core $U = 17$ km yr^{-1} (e.g. Gillet *et al.* 2015; Aubert 2015; Bärenzung *et al.* 2018), root-mean-squared magnetic field intensity $B = 4$ mT (Gillet *et al.* 2010), $\rho = 11\,000$ kg m^{-3}, $D = 2260$ km, $\mu = 4\pi\ 10^{-7}$ H m^{-1}, $\Omega = 7.29\ 10^{-5}$ 1 s^{-1} and a range $\eta = 0.5 - 3$ m^2 s^{-1} for magnetic diffusivity (Pozzo *et al.* 2012; Konôpková *et al.* 2016).

	Mag. diffusion	Overturn	Alfvén	Rotational
	$\tau_\eta = D^2/\eta$	$\tau_U = D/U$	$\tau_A = \sqrt{\rho\mu}D/B$	$2\pi\tau_\Omega = 2\pi/\Omega$
71p model	135 000 yr	119 yr	5.8 yr	11.8 d
Earth's core	5×10^4–3×10^5 yr	133 yr	2.1 yr	1 d

(2019). To this end a catalogue of 14 prominent jerk events was constructed during the integration of this new model. This paper is organized as follows: Section 2 introduces the numerical model, the jerk catalogue, and recalls a few important previous results. The analysis of the catalogue is presented in Section 3, and discussed in comparison with the geomagnetic observations in Section 4.

2 MODEL AND METHODS

2.1 Description of the numerical model

We use the output from the numerical model case previously presented in AG21, with full details on the equation set and numerical method being provided in Aubert *et al.* (2017). We consider a spherical coordinate system (r, θ, φ) with unit vectors $\mathbf{e}_r, \mathbf{e}_\theta, \mathbf{e}_\varphi$. The model numerically solves for Boussinesq convection, thermochemical density anomaly transport, and magnetic induction in the magnetohydrodynamic approximation, within an electrically conducting and rotating spherical fluid shell of thickness $D = r_o - r_i$ and aspect ratio $r_i/r_o = 0.35$ representing the Earth's outer core. The shell surrounds a solid inner core of radius r_i, and is surrounded by a solid mantle between radii r_o and $r_E = 1.83 r_o$ (the surface of the Earth). Our unknown fields are the velocity field $\mathbf{u}$, magnetic field $\mathbf{B}$ and the density anomaly field. Mechanical boundary conditions for $\mathbf{u}$ at r_i and r_o are of stress-free type. Thermochemical boundary conditions for density anomaly are of the fixed-flux type, with the system being forced at $r = r_i$ by a mass anomaly flux F and buoyancy being neutral at $r = r_o$ (vanishing mass anomaly flux). Lateral heterogeneities are also superimposed at both boundaries on top of these homogeneous mass anomaly fluxes, respecting the set-up adopted in Aubert *et al.* (2013). Electromagnetic boundary conditions are of the conducting type for the magnetic field $\mathbf{B}$. The electrical conductivities of the inner and outer core are set to the same value $\sigma = 1/\mu\eta$, with μ the magnetic permeability and η the magnetic diffusivity. The mantle features a thin conducting layer at its base, of thickness Δ and conductivity σ_M. Angular momentum balance is exchanged in the coupled outer core–mantle–inner core system through electromagnetic coupling at both boundaries of the fluid shell, and gravitational coupling between the inner core and the mantle. As a result, the inner core and mantle present differential axial rotations with respect to the outer core, and the ensemble rotates at the constant planetary rate $\mathbf{\Omega}$. The four main dimensionless parameters are the flux-based Rayleigh, Ekman, Prandtl and magnetic Prandtl numbers:

$$Ra_F = \frac{g_o F}{4\pi\rho\Omega^3 D^4},\ E = \frac{\nu}{\Omega D^2},\ Pr = \frac{\nu}{\kappa},\ Pm = \frac{\nu}{\eta}. \tag{1}$$

Here g_o is gravity at the core surface, ρ is the outer core density, ν and κ are the viscous and thermochemical diffusivities. We have previously shown (Aubert *et al.* 2017) that these four parameters can be connected to a single variable that describes the position along a parameter space path to Earth's core. This path bridges the gap between previously accessible physical conditions where many numerical simulations have been computed, and the extreme conditions of Earth's core. The model used here is located at 71 per cent of this path (the 71p model, AG21). This represents an improvement, respectively, to the model of Aubert & Finlay (2019), which was located at 50 per cent of this path. Parameters values for the 71p model path are

$$Ra_F = 2.7 \times 10^{-10},\ E = 3 \times 10^{-10},\ Pr = 1,\ Pm = 7.9 \times 10^{-3}. \tag{2}$$

The numerical method rests on a decomposition of $\mathbf{u}$, $\mathbf{B}$ and density anomaly in spherical harmonics up to degree and order ℓ_{max} varying between 133 and 170 during the run sequence (see AG21), and a discretization in the radial direction on a second-order finite-differencing scheme with $NR = 1248$ gridpoints. We use the spherical harmonics transform library SHTns (Schaeffer 2013) freely available at `https://bitbucket.org/nschaeff/shtns`. The dimensionless parameter values reported above imply already extreme numerical conditions for the 71p model, that can be simulated at this spatial resolution through the help of an approximation involving a smoothly ramping hyperdiffusivity applied on the velocity and density anomaly fields, but not on the magnetic field that remains fully resolved. The details and physical validation for this approximation are presented in Aubert *et al.* (2017) and AG21. Like all other models previously studied along the parameter space path, the 71p model produces a self-sustained, dipole-dominated magnetic field of Earth-like geometry (Christensen *et al.* 2010) that did not reverse polarity during the 14-kyr-long integration time.

Here we also recall secondary equations and dimensionless parameters that relate to angular momentum exchanges between the core, mantle and inner core. The dimensionless mantle conductance is set to $\Delta\sigma_M/D\sigma = 10^{-4}$, at the mid-point, in logarithmic space, of geophysical estimates (Pichon *et al.* 2016). We adopt a simplified long-term formulation for gravitational coupling between inner core and mantle (Aubert & Dumberry 2011; Aubert *et al.* 2013). The gravitational torque exerted on the mantle by the inner core is written $\Gamma_G = -\Gamma\tau(\Omega_M - \Omega_I)$, where $\Gamma\tau$ is a coupling constant, and $\Omega_{I,M}$ are, respectively, the inner core and mantle axial rotation rates. The corresponding dimensionless quantity for gravitational coupling is set to $\Gamma\tau/\rho D^5\Omega = 0.75$, a value at which the indirect coupling between the outer core and the mantle via the inner core dominates the direct coupling at the core–mantle boundary (Pichon *et al.* 2016). The mantle rotation rate evolves according to

$$I_M \frac{d\Omega_M}{dt} = \Gamma_M + \Gamma_G, \tag{3}$$

where t is time, I_M is the moment of inertia of the mantle and the magnetic torque at the core–mantle boundary is given by

$$\Gamma_M = -\frac{r_o}{\mu}\int_{r=r_o} (\mathbf{B}\cdot\mathbf{e}_r)(\mathbf{B}\cdot\mathbf{e}_\varphi)\sin(\theta)\,dS. \tag{4}$$

Note that similar equations also determine the differential rotation of the inner core (Pichon *et al.* 2016). In this study we consider mantle differential rotation through the associated temporal rate of change in the length-of-day (LOD) given by (Jackson *et al.* 1993; Jault *et al.* 1988)

$$\frac{\mathrm{d(LOD)}}{\mathrm{d}t} = -\frac{2\pi}{\Omega^2}\frac{\mathrm{d}\Omega_\mathrm{M}}{\mathrm{d}t}. \tag{5}$$

The model solves for variables in dimensionless form, after which these variables are cast back to a dimensional form by using a set of rescaling procedures that take advantage of the main force equilibria that are preserved along the parameter space path (see a detailed discussion in Aubert 2020). Length scales are dimensioned by setting $D = 2260$ km as Earth's outer core thickness. Dimensional times are obtained by setting the magnetic diffusion time to $\tau_\eta = D^2/\eta = 135000$ yr, corresponding to a dipole decay time $r_o^2/\pi^2\eta \approx 32400$ yr. The velocity field $\mathbf{u}$ and Alfvén velocity $\mathbf{B}/\sqrt{\rho\mu}$ expressed in units of η/D are dimensioned using the choices made above. The root-mean-squared magnetic intensity inside the shell is set to the Earth estimate $B = 4$ mT (Gillet *et al.* 2010) in order to present magnetic fields in dimensional units. This choice also ensures a realistic amplitude of the magnetic field at the core surface, because the ratio of surface to deep field amplitude is about correct (Aubert *et al.* 2017). As mentioned in AG21, different choices need to be made for the Alfvén velocity and magnetic intensity, despite the two involving the same variable. This stems from the fact that the model is not yet at the end of the path, where the two choices exactly converge. Given the proximity of the current model to this end, this is not a serious concern, and the choice made here has the advantage of providing an easy extrapolation of the results to core conditions, where the magnetic intensity remains the same and Alfvén velocities should only be multiplied by a factor 2.76 (see Table 1). Finally, dimensionless density anomalies expressed in units of $\rho\Omega\eta/g_oD$ are dimensioned using the choice made for η above and Earth estimates of the other variables (see again AG21).

2.2 Key timescales, hierarchy of force balances and rapid hydromagnetic waves

Table 1 presents the key dimensional timescales of the 71p model and compares their values to those expected in Earth's core. The design of the parameter space path (Aubert *et al.* 2017) implies that the magnetic diffusion and core overturn times match the Earth estimates, such that the magnetic Reynolds number $Rm = \tau_\eta/\tau_U \approx 10^3$ of the model is realistic. Along the parameter space path, too, values of τ_A and τ_Ω gradually converge towards their estimates for Earth's core. Table 1 shows that the Alfvén timescale of the 71p model is within a factor 2.76 of the Earth estimate. The high Lundquist number $S = \tau_\eta/\tau_A \approx 2.3 \times 10^4$ of the model ensures a weak effect of magnetic diffusion on Alfvén waves (AG21). Likewise, the length of the numerical day $2\pi\tau_\Omega$ is roughly within a factor 10 away from the Earth value, meaning that rotational control on Alfvén waves is enforced in the model as in Earth's core since $\tau_A \gg \tau_\Omega$.

The hierarchy of timescales presented in Table 1 corresponds to an amplitude hierarchy of successive force balances in the system. The slow (secular) convective evolution on timescale τ_U is generally governed by the so-called QG-MAC balance between the Coriolis, pressure, Lorentz and buoyancy forces (Schwaiger *et al.* 2019). Intermittent deviations from this balance are necessarily compensated by inertia, which is the next force in the hierarchy and, in the conditions of the 71p model and Earth's core, comes several orders of magnitude below these primary forces (Aubert 2019; AG21). These deviations lead to the generation of hydromagnetic magneto-inertial waves (Aubert 2018; Aubert & Finlay 2019; AG21), the subsequent propagation of which causes rapid flow and magnetic acceleration signals at the core surface on an interannual timescale $\tau_A \ll \tau_U$. These waves include fully geostrophic torsional Alfvén waves with an axisymmetric and axially columnar structure that cancels out the influence of the Coriolis force. They further comprise non-axisymmetric waves that are quasi-geostrophic (QG) in the sense that they also mitigate the Coriolis force by acquiring an axially columnar structure but cannot completely offset its influence as in the case of axisymmetric torsional waves. Gillet *et al.* (2022b) have established an idealized plane-wave dispersion relationship for QG hydromagnetic waves that captures a number of interesting properties, which are recalled here. In the case where the strongest spatial gradients of the wave pattern are in the cylindrical radial direction, this relationship can be written:

$$\omega = \frac{1}{(kH)^2}\left(m\Omega \pm \sqrt{(m\Omega)^2 + (V_A k^3 H^2)^2}\right). \tag{6}$$

Here $V_A \approx D/\sqrt{3}\tau_A$ is the Alfvén velocity relative to the cylindrical radial component of the background field, m is the azimuthal mode number, k the cylindrical radial wave number and H the half-height of the fluid columns. In a small radial wavelength limit $V_A k^3 H^2 \gg m\Omega$ the cylindrical radial component of the group velocity is approximated by

$$c_g = \frac{\partial\omega}{\partial k} \approx \pm V_A - \frac{2m\Omega}{k^3 H^2}. \tag{7}$$

Close to the point where the QG-MAC balance is disrupted, a magneto-inertial wave balance can therefore dominate the residual Coriolis force on the columnar wave fronts if the wavenumber k is large enough (small enough radial wavelengths), such that propagation speeds close to V_A are observed, and the waves can be categorized as quasi-geostrophic Alfvén (QGA) waves (Aubert 2018). Significant slowdowns in the cylindrical radial propagation speed can be observed for outward-propagating waves as H decreases and the topographic 'beta' effect of the Coriolis force increases (AG21). In this case, the waves gradually transition to a QG magneto-Coriolis balance (QGMC, Gerick *et al.* 2021). QGMC waves can be found in the same interannual timescale range as QGA waves (Gerick *et al.* 2021), such that the typical period can be preserved across the transition. In addition to wave slowdown, the appearance of dispersion according to eq. (7) is another manifestation of the transition from QGA to QGMC, with the waves slowing down the least being of smaller radial, and larger azimuthal wavelength.

The interannual signals caused by these quasi-geostrophic hydromagnetic waves have been shown to account for a number of observational properties of recent jerk events (Aubert & Finlay 2019). In particular, they clarify the need for non-axisymmetric, rapid core surface flow accelerations to produce the geomagnetic variations in the vicinity of jerks (e.g. Wardinski *et al.* 2008; Silva & Hulot 2012; Kloss & Finlay 2019). The hypothesis of rapid, non-axisymmetric, hydromagnetic waves to explain jerks builds upon the downward re-evaluation of the Alfvén timescale to $\tau_A \approx 2$ yr introduced by Gillet *et al.* (2010) based on the observation of torsional waves in Earth's core. This value is also consistent with the estimated convective power available to the geodynamo, in the framework of the path theory (Aubert *et al.* 2017). Prior to that, Alfvén waves had been recognized as the part of core dynamics with the potential to explain jerks (Bloxham *et al.* 2002), but the focus was on axisymmetric (torsional) waves and it was thought (e.g. Zatman & Bloxham 1997) that the Alfvén time and wave period would be 10

times larger than the value proposed by Gillet *et al.* (2010). It was also believed that the Coriolis force would preclude the possibility to observe interannual non-axisymmetric Alfvén waves at large scales (e.g. Lehnert 1954; Hide 1966), such that only slow MC waves with secular and longer periods could exist at this level. The relationship (eq. 7) illustrates how this can be circumvented at sufficiently small (cylindrical radial) wavelengths. For further details on the connections between interannual geomagnetic variations, waves in the core and in numerical simulations, the reader may consult the recent review of Gillet *et al.* (2022a). Here we will focus on specific situations where waves naturally forced by convection reach high amplitudes and compare the resulting magnetic signals to the characteristics of observed geomagnetic jerks.

2.3 Jerk catalogue

2.3.1 Time-series of the 71p model and characterization of simulated jerk events

The time-series from the 71p model spans 14 000 yr dimensional time. Among the relevant diagnostics that have been stored during the run sequence (see AG21), we specifically analyse the time derivatives of the magnetic field, the secular variation (SV) $\dot{\mathbf{B}} = \partial \mathbf{B}/\partial t$ and acceleration (SA) $\ddot{\mathbf{B}} = \partial^2 \mathbf{B}/\partial t^2$. As in Aubert & Finlay (2019), simulated jerks are characterized with the help of the Earth surface SA energy

$$E_{\rm SA}(t) = \frac{1}{S_{\rm E}} \int_{S_{\rm E}} \ddot{\mathbf{B}}^2(r_{\rm E}, \theta, \varphi, t)\, {\rm d}S = \left\langle \ddot{\mathbf{B}}^2 \right\rangle_{S_{\rm E}}, \tag{8}$$

where we introduce angle brackets for averages over spherical surfaces and $S_{\rm E}$ is Earth surface at radius $r_{\rm E}$. We similarly define the jerk energy

$$E_{\rm J}(t) = \left\langle \left(\left[\ddot{\mathbf{B}}\right]_t^{t+\Delta t} - \left[\ddot{\mathbf{B}}\right]_{t-\Delta t}^{t} \right)^2 \right\rangle_{S_{\rm E}}, \tag{9}$$

where the square brackets stand for time averaging and $\Delta t = 3$ yr is a running averaging time that has proved useful for studying global variations in the secular acceleration (e.g. Chulliat & Maus 2014; Aubert & Finlay 2019; Finlay *et al.* 2020). To compute these two quantities, the magnetic field is retained up to spherical harmonic degree and order 13, which captures most of the energy at Earth's surface. Fig. 1 presents the time-series of $E_{\rm SA}$ and $E_{\rm J}$ during the 71p model sequence. An observable jerk is characterized by rapid and simultaneous increases in the amplitude of both quantities $E_{\rm SA}$ and $E_{\rm J}$ significantly (here more than three times) above their time-average levels $[E_{\rm J}] \approx [E_{\rm SA}] \approx 30$ nT^2 yr^{-4} (green zones in Fig. 1). This occurs when there is a step change in the secular acceleration that significantly exceeds its typical level, (the classical definition of a geomagnetic jerk), and when the secular acceleration itself also exceeds its typical level (as is the case for jerks in the satellite era, Chulliat *et al.* 2010). A set of 14 jerk events have been selected that way, containing events at least of typical satellite-era strength (i.e. $E_{\rm J} \sim 100$ nT^2 yr^{-4}, about three times stronger than the time-averaged value) as well as significantly stronger events with $E_{\rm J}$ up to about 800 nT^2 yr^{-4} (see Table 2). In addition to containing events of varying strength, the catalogue also explores varying durations, morphologies, and, as we shall see, also samples a variety of physical situations where magneto-inertial dynamics leading to jerk signals arises. Within the catalogue, event 5 has been further subdivided into three phases 5a,b,c because of its complexity. For computational reasons, the numerical model does not systematically store outputs relative to the internal structure. For each selected event, a model rerun has therefore been performed to retrieve these outputs. Events creating a SA pulse but no discernable pulse in $E_{\rm J}$ have been discarded in order to focus on events whose SA changes can easily be followed in observations. Events corresponding to numerical artefacts (change of time step or other numerical instability, see AG21) have also been discarded.

2.3.2 Diagnostics of simulated jerks

Table 2 summarises a set of quantitative and qualitative diagnostics obtained from the 71p model time-series. Similar diagnostics are also extracted from the main jerk event studied in Aubert & Finlay (2019). The diagnostics are described below:

(i) '#' is the jerk reference number, followed by 'Time', the simulation time at which it occurs.

(ii) 'Duration' is an approximate event duration over which $E_{\rm SA}(t)$, $E_{\rm J}(t)$ significantly exceed their time-average levels (green regions in Fig. 1).

(iii) The next two columns provide details on the geographical localization of the SA pulses corresponding to jerk events. First, 'Lat.' is the latitude at which these pulses are found in representation of the core surface radial SA up to spherical harmonic degree 13 (see Aubert & Finlay 2019). Here 'high' means latitudes above 45°, 'mid' means latitudes between 20° and 45°, and 'low' means latitudes below 20°. The distribution of jerk latitudes in the catalogue is representative of the long-term distribution in the 71p model (AG21).

(iv) At the Earth surface, the signature of these radial SA pulses usually consists of several intense and large-scale patches that rapidly alternate their polarity in time. 'Region' provides the approximate longitudinal localization of these patches.

(v) 'Multi (time)' is a binary qualification of whether the event has at least two peaks in $E_{\rm J}$ overcoming a threshold of 100 nT^2 yr^{-4}. When labelled yes, that is 'Y' this generally corresponds to SA changes of alternating polarity. There are generally no multiple alternations in events with a duration shorter than 20 yr.

(vi) 'Globality' is a quantitative measure of the visibility of jerks as 'V-shape' structures (as introduced in Section 1) in time-series of the Earth surface SV at given locations. See Section 2.3.3 for details.

(vii) 'Drift' is a qualification of the longitudinal direction (E or W, when present) of a coherent azimuthal drift of structures observed on time-longitude plots of the core surface radial SA up to spherical harmonic degree 9 and after filtering in time with a 3-yr moving average. These two filtering steps are designed to reflect the spatio-temporal resolution that can easily be reached in geomagnetic field models of the SA.

(viii) 'Trigger' is a categorization of the physical nature of the jerk trigger. This is obtained in relationship with the W/C quantitative indicator (see next item) and visual inspection of movie sequences for flow acceleration, density anomaly, magnetic field inside the shell. DW stands for 'Deep Wave origin', that is emission of hydromagnetic QGA waves in the cylindrical radial direction from a deep convective plume rooted at the inner core boundary, and subsequent propagation towards the core surface at low latitudes, similarly to the mechanism first explained in Aubert & Finlay (2019). SW stands for 'Shallow Wave origin', that is emission of hydromagnetic waves at low latitude close to the core surface. SC stands for 'Shallow Convection', where jerks are triggered at the high-latitude imprint of a deep convective structure.

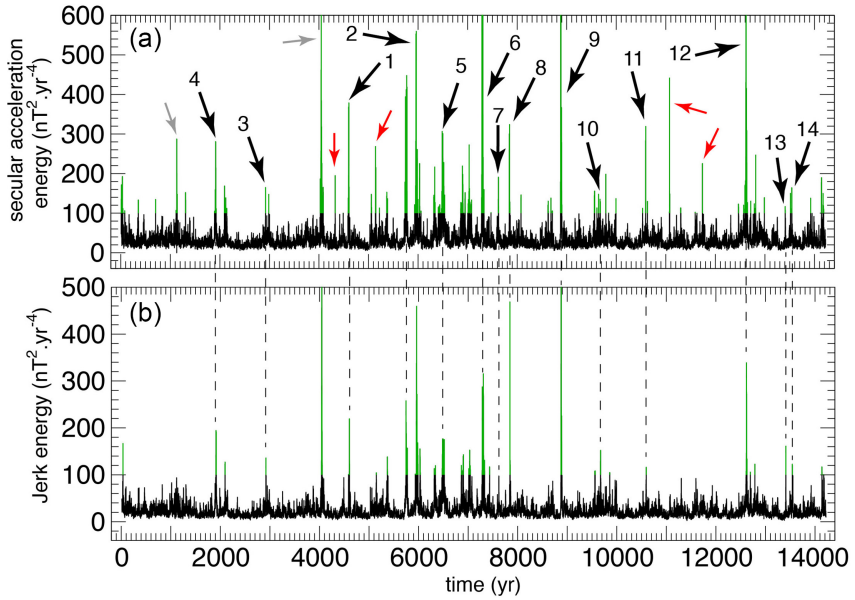

Figure 1. Magnetic acceleration energy E_{SA} (top panel) and jerk energy E_J (bottom panel) at Earth surface, as functions of the dimensional simulation time. Green regions where $E_{J,SA} > 100$ nT^2 yr^{-4} highlight the notable jerk events. Numbered black arrows locate the 14 high-amplitude jerks analysed in this study. Red arrows locate jerks that have not been selected because they occur too fast to be discernable once the 3-yr moving averaging is performed to compute E_J. Grey arrows locate numerical artefacts that have also been discarded in our selection.

(ix) W/C (Waves over Convection) is a quantitative indicator of the relative importance of short versus long timescale dynamics in the jerk events, or of the relative roles played by rapid hydromagnetic waves and slow convection. This diagnostic also assesses disruptions to the QG-MAC balance at the core surface. See Section 2.3.4 for details.

(x) E_J^{max} is the maximum value of the jerk energy reached during the event.

(xi) E_J^{max}/E_{SA}^{max} compares the maximum jerk energy to the maximum energy of SA pulses involved in the event.

(xii) SVS is an indicator of the amplitude of possible surges in the SV at Earth surface associated with the jerk event (e.g. Jackson & Finlay 2015). The r.m.s. Earth surface SV amplitude is computed as $A_{SV}(t) = \left\langle \dot{\mathbf{B}}^2 \right\rangle_{S_E}^{1/2}$, and the quantity SVS is defined as

$$\mathrm{SVS} = \frac{\Delta A_{SV}}{\mathrm{std}(A_{SV})}, \tag{10}$$

where ΔA_{SV} is the variation in A_{SV} observed during the event (which can be positive or negative), and $\mathrm{std}(A_{SV}) = 20.3$ nT yr^{-1} is a standard deviation computed for the whole time span of the 71p model.

(xiii) MFS is an indicator of the large-scale visibility of possible surges in the core surface magnetic field amplitude, that is large-scale flux expulsion during jerk events. The r.m.s, large-scale core surface magnetic energy is computed as $A_{MF}(t) = \left\langle \mathbf{B}^2_{\ell \le 13} \right\rangle_{S_{CMB}}^{1/2}$, where S_{CMB} is the spherical surface of the CMB and the core surface magnetic field is truncated at spherical harmonic degree and order 13. The quantity MFS is defined as

$$\mathrm{MFS} = \frac{\Delta A_{MF}}{\mathrm{std}(A_{MF})}, \tag{11}$$

where ΔA_{MF} is the variation in A_{MF} observed during the event, and $\mathrm{std}(A_{MF}) = 0.034$ mT is computed for the whole time span of the 71p model.

(xiv) 'LOD' indicates whether there is a visible signal in the length-of-day time-series associated to the jerk event. Jerks can indeed cause pulses in the acceleration $\mathrm{d}^2\Gamma_M/\mathrm{d}t^2$ of the magnetic torque exerted by the core on the mantle (see Aubert & Finlay 2019). If these pulses significantly exceed the level of the gravitational torque acceleration $\mathrm{d}^2\Gamma_G/\mathrm{d}t^2$ during the event, then a rapid inflexion is created in $\mathrm{d(LOD)}/\mathrm{d}t$ (eqs 3 and 5) and the LOD indicator is 'Y'.

2.3.3 Detectability and quantitative assessment of V-shaped secular variation patterns.

As discussed in Section 1, the presence of 'V-shapes', or abrupt slope changes between decadal piecewise linear trends in SV time-series at Earth surface, is the most studied observational characteristic of geomagnetic jerks. Here we mostly analyse the East component of the magnetic field for direct comparison with the Y component of observatory time-series that often presents the best visible and least noisy V-shapes during known observatory-era jerks, particularly in Europe (e.g. Wardinski & Holme 2011). To detect the presence of V-shapes and quantify their importance in the simulated jerk events, we use two methods that reflect the varying degree of knowledge provided by ground observatory and satellite measurements.

Method 1 assumes knowledge of global secular acceleration at Earth's surface, as provided by satellite geomagnetic field models. We first extract decadal trends in the SV that relate to slow core convection by smoothing the SA over windows of 10 yr (the typical timescale for magnetic acceleration of convective origin in the model and the geomagnetic field, Aubert 2018, AG21). Significant interruptions in these decadal trends are then evaluated by computing the r.m.s. value $\Delta SA(t)$ of changes in the smoothed eastward SA:

$$\Delta SA_\varphi(t) = \left\langle \left([\ddot{\mathbf{B}} \cdot \mathbf{e}_\varphi]_t^{t+10\ \mathrm{yr}} - [\ddot{\mathbf{B}} \cdot \mathbf{e}_\varphi]_{t-10\ \mathrm{yr}}^{t} \right)^2 \right\rangle_{S_E}^{1/2}. \tag{12}$$

We extract the times t_i where $\Delta SA_\varphi(t)$ reaches its maxima, and define the maximal smoothed local SA change for the event among

Table 2. Diagnostics of simulated jerks events 1–14 from the 71p model, and the AF19 event (Aubert & Finlay 2019). See text for details.

#	Time (yr)	Duration (yr)	Lat.	Region	Multi. (time)	Globality (per cent)	Drift	Trigger	W/C	E_J^{max} $\left(\mathrm{nT^2.yr^{-2}}\right)$	$\frac{E_J^{max}}{E_{SA}^{max}}$	SVS	MFS	LOD
1	4605	50	low	India	Y	47		SW	1.6	232	0.56	1.0	1.2	
2	5750	60	low	India, America	Y	50	W	SW	1.2	282	0.63	1.7	0.7	
3	2920	20	low	Africa, Pacific	Y	33	E/W	DW	1.7	143	0.86	0.3	0.1	
4	1915	30	low	India, Atlantic	Y	30	E/W	DW	2.2	201	0.71	1.0	0.0	
5a	6485		low	Africa			W	DW	1.6	202	0.64	–2.2	0.2	
5b	6500	a-c: 50	high	Antarctica	a-c: Y	a-c: 46		SC	0.9	213	0.70	0.2	0.2	
5c	6520		low	India			E/W	SW	1.1	204	0.86	0.6	0.2	
6	7295	40	low	Africa, Pacific	Y	64		SW	1.6	344	0.10	2.9	1.6	Y
7	7620	10	low	India, Atlantic		19	W	SW	1.3	122	0.60	0.3	0.1	
8	7844	20	high	Australia	Y	50		SC	1.2	495	1.49	0.4	0.1	
9	8878	30	low	India, Pacific	Y	66	W	SW	1.3	806	0.28	3.2	1.0	Y
10	9673	20	high	Arctic		37		SC	0.8	162	1.12	–0.7	–0.1	
11	10 593	10	mid	Pacific		21		SW	1.5	129	0.39	0.7	0.1	
12	12 619	50	low	India, Africa	Y	43		SW	1.0	426	0.59	0.6	0.0	Y
13	13 412	10	low	India		19		SW	1.5	171	1.42	0.3	0.0	
14	13 543	30	low	India	Y	42		DW	1.8	137	0.83	0.4	–0.2	
AF19		10	low	Africa		44	W	DW	1.9	103	0.88	0.2	0.0	

these times t_i as

$$J_\varphi(\theta,\varphi) = \max\left(\left|[\ddot{\mathbf{B}}\cdot\mathbf{e}_\varphi]_t^{t+10\ \mathrm{yr}} - [\ddot{\mathbf{B}}\cdot\mathbf{e}_\varphi]_{t-10\ \mathrm{yr}}^{t}\right|(r_E,\theta,\varphi,t_i)\right), \tag{13}$$

and compare this to the local r.m.s eastward SA, smoothed over 20 yr and averaged over the event:

$$SA_\varphi(\theta,\varphi) = \sqrt{\left[\left([\ddot{\mathbf{B}}\cdot\mathbf{e}_\varphi]_{t-10\ \mathrm{yr}}^{t+10\ \mathrm{yr}}\right)^2(r_E,\theta,\varphi,t)\right]_{\mathrm{event}}}. \tag{14}$$

We finally define our first detectability diagnostic $\chi(\theta,\phi)$ for V-shapes in the event as

$$\chi(\theta,\phi) = J_\varphi(\theta,\varphi)/SA_\varphi(\theta,\varphi). \tag{15}$$

This diagnostic can be analysed location by location to assess the sharpness of V-shapes independent of the local strength of the secular acceleration, together with the global synchronicity of V-shapes around times t_i (see Section 3.4). We also subjectively assess the 'Globality' of jerk events by reporting in Table 2 the percentage of Earth surface over which $\chi(\theta,\phi) > 3$. Diagnostics similar to eqs (12–15) can also be derived for the radial and meridional components of the field, but we note that the global occurrence times t_i are the same across components because these all derive from the same potential outside the core.

Method 2 does not require particular differentiability properties of the field and only assumes knowledge of time-series at given locations of the Earth surface, as provided at ground observatories. At a given location (θ,φ), we sample $\mathbf{B}\cdot\mathbf{e}_\varphi$ at yearly intervals over a 400-yr period centred at the time of an event t^*, mimicking the annual-means data from observatory records commonly used to find jerks, from which we compute the SV time-series. Then we quantify the fit of pronounced 'V' shapes to these time-series by entering the discrete SV dataset into a Bayesian method described in Livermore *et al.* (2018). By computing the posterior distribution of the SV time-series assuming an underlying piecewise linear model, this allows us to quantify which points in the time-series are best described by an abrupt change in slope of consecutive linear segments, the classical definition of a jerk. Our transdimensional method differs from previous studies that typically applied two-segment fits on short data windows (Pinheiro *et al.* 2011; Brown *et al.* 2013), as we allow a many-segment piecewise-linear time-series to describe our 400-yr SV record, where the number and length of the linear segments are unknown but are selected by the data as part of the modelling. No regularization is needed as the Bayesian framework will always guarantee parsimonious solutions where the data allow (Sambridge *et al.* 2006). The method requires specification of the prior distribution of various quantities: the prior for the SV is assumed to be of uniform probability over $[-400, 400]$ nT yr^{-1}, and that of the number of linear segments is uniform over the interval [0,100]. The likelihood is assumed to be normally distributed with a standard deviation (representing both data and model uncertainty) taken to be 10 per cent of the maximum range in SV over the time window.

The posterior distribution is approximated numerically by a large ensemble of $N = 10^5$ models of piecewise linear fits $f_i(t)$, $1 \le i \le N$ to the SV, thinned from a supersample of size 10^8. Using the ensemble members we can derive the quantity $\delta_j = \mathrm{mean}_i(|\Delta f_i(t)|)$, the posterior average absolute change in slope of SV within a certain time bin $[t_j, t_{j+1}]$. Note that the only times that contribute to the sum are those at a change point of the piecewise linear functions f_i. High values of δ_j correspond to time bins in which many ensemble members contain a change in slope which is large: that is, significant evidence for a jerk. We choose time bins of width 20 yr (same as method 1). At each location, we finally normalize δ_j by the average value over the time bins to find our second detection diagnostic:

$$\mathcal{S}(\theta,\varphi) = \delta_*/\mathrm{mean}_j(\delta_j), \tag{16}$$

where the star indicates the bin containing the jerk event at $t = t^*$. Here this bin is selected based on information from E_J time-series. We will relax this in a forthcoming study, to also assess the timing of jerks as an outcome of the method.

2.3.4 *Quantitative assessment of disruptions to the QG-MAC balance and the roles played by waves and convection in the jerk events*

Introducing the core flow acceleration $\dot{\mathbf{u}} = \partial\mathbf{u}/\partial t$, it is useful (e.g. Lesur *et al.* 2010; Aubert 2018) to break down the magnetic induction equation at the core surface according to

$$\ddot{\mathbf{B}} = \nabla\times(\dot{\mathbf{u}}\times\mathbf{B}) + \nabla\times(\mathbf{u}\times\dot{\mathbf{B}}) + \eta\boldsymbol{\Delta}(\dot{\mathbf{B}}). \tag{17}$$

For each term in the radial component of eq. (17), we compute the following mean squared values over the core surface, retained up to spherical harmonic degree 13 and averaged over the event duration:

$$W = \left[\left\langle(\nabla\times(\dot{\mathbf{u}}\times\mathbf{B})\cdot\mathbf{e}_r)^2_{\ell\le13}\right\rangle\right]_{\mathrm{event}}, \tag{18}$$

$$C = \left[\left\langle(\nabla\times(\mathbf{u}\times\dot{\mathbf{B}})\cdot\mathbf{e}_r)^2_{\ell\le13}\right\rangle\right]_{\mathrm{event}}, \tag{19}$$

and we similarly define quantities T for the total secular acceleration and Di for the diffusive contribution. As we illustrate below, the quantity W may be interpreted as the contribution from inertia-bearing waves to the jerk event, while C represents the contribution from inertia-less convective dynamics. In a typical evolution of the system under the QG-MAC force balance, the timescales determining the magnitude of $\dot{\mathbf{u}}$ and $\dot{\mathbf{B}}$ are both commensurate with the overturn time τ_U, leading to $W/C \approx 1$, usually with a sizeable cancellation between the two inductive terms in eq. (17) (Aubert 2018), as a manifestation of Lenz's law. If the QG-MAC balance is disrupted, then the inertial compensation involves rapid inertia-bearing waves of typical timescale τ_A. Such waves significantly enhance $\dot{\mathbf{u}}$ and the associated contribution W from flow acceleration to the secular acceleration budget (Aubert 2018), but only weakly perturb $\mathbf{u}$, $\mathbf{B}$, $\dot{\mathbf{B}}$ (AG21), resulting in $W/C > 1$. Conversely, events with $W/C < 1$ are representative of convection-driven dynamics with a rapid evolution in $\mathbf{B}$, without a significant inertial compensation of the QG-MAC balance. In summary, the departure of W/C above unity quantifies the deviation from the QG-MAC balance, while the position of W/C relative to unity characterizes the relative role of waves and convection in each jerk event.

3 RESULTS

3.1 A taxonomy of jerk mechanisms

Two types of dynamic mechanisms have been identified across the 16 individual events of the catalogue (breaking event 5 into three subevents). The first and most frequent type, found in 13 instances, involves hydromagnetic wave dynamics following a local disruption of the QG-MAC balance, and leads to jerk signatures found at low to mid-latitudes (diagnostic 'Lat' in Table 2). Among these events, we further distinguish these where the disruption originates at depth in the core (deep wave trigger labelled as DW in Table 2), or near the core surface (shallow wave or SW trigger). This distinction

corresponds to an interesting variability in the dynamics involved in the events, and also in their strength, with DW events having E_J up to 200 nT^2/yr^4, typically weaker than SW events (Table 2). The second type of jerk mechanism, found in the remaining three instances, involves the interaction, near the core surface and preferentially at high latitudes, of intense convection with intense magnetic field found at the same location (events 5b, 8 and 10, trigger labelled as shallow convection or SC in Table 2).

The first quantitative element supporting this taxonomy is the examination in Fig. 2 of contributors to the secular acceleration at the core surface (eq. 17), together with the integral W/C diagnostic. Fig. 2(a) uses event 3 as an example of the typical situation encountered during deep wave events (which also include the jerk simulation of Aubert & Finlay 2019). The wave contribution W brought by the interaction of flow acceleration $\dot{\mathbf{u}}$ and the background magnetic field $\mathbf{B}$ provides most of the energy of the secular acceleration pulse of the event. Accordingly, DW events feature W/C ratios elevated to or above 1.6 (Table 2). This indicates a primary role of SA induction caused by flow acceleration (or inertia), that further shows an inertial compensation of the QG-MAC balance and a prominent role of the hydromagnetic waves that contribute significantly to this acceleration (AG21). Maps of the SA contributors presented in Fig. 2(a) also confirm the low-latitude character of DW events.

The other end-member is provided by shallow convection events such as event 10 (Fig. 2c), which are found at high latitudes. Here it is the contribution C from the interaction of the flow $\mathbf{u}$ with the SV $\dot{\mathbf{B}}$ that dominates the budget during most of the event (though at times largely cancelling with the other contribution, indicating an effect of Lenz's law), leading to W/C=0.8 in this instance, and W/C values close to or below 1 for the other SC events. This contribution stems from the presence of intense flow and strong magnetic field (hence intense SV also) at the same location in space (here within the northern polar vortex), which leads to rapid convective advection of SV features near the core surface. Hydromagnetic waves are not observed in these SC events, confirming that they unfold primarily through convection under the QG-MAC balance, without specifically involving a disruption and inertial compensation. SC events are rare because the co-existence of strong velocities and magnetic fields is in contradiction with the distribution promoted by Lenz's law in the system (Aubert 2019). Here they are further prevented by the neutral buoyancy which is prescribed at the core surface in the 71p model.

Shallow wave events such as event 9 (Fig. 2b) blend the characteristics of the two above end-members, and feature values of W/C between 1 and 1.6 (Table 2). They indeed correspond to the arrival of buoyancy plumes at low latitudes near the core surface, with additional wave emission. The two contributors to the secular acceleration rapidly alternate in strength, leading to an apparent rapid rotation of the large-scale pairs of radial SA patches at the core surface. Because of the proximity of the source to the core surface, these SW events provide the strongest jerks in the catalogue. Finally, irrespectively of the event type, Fig. 2 shows that magnetic diffusion (with contribution Di) is irrelevant to their dynamics.

3.2 Dynamics of wave-driven events

At this point, we focus on the most frequent type of events, that is those involving a disruption to the QG-MAC balance and hydromagnetic wave propagation, and complete the taxonomy proposed above with a examination of the dynamics involved in these events. In the examples below, this disruption to the leading-order force balance is of buoyant (Fig. 3), or magnetic origin (Fig. 4). The Coriolis and pressure forces, on the other hand, are not expected to play a triggering role but rather only constrain the subsequent dynamics.

To recall the typical behaviour found in deep wave events, as initially observed in Aubert & Finlay (2019), the flow acceleration, magnetic and density anomaly field structures of event 3 are shown in Fig. 3. Here we refine the description of these events by additionally taking advantage of the new insights brought by the recent work of Gerick *et al.* (2021), Gillet *et al.* (2022b) and AG21, summarized in Section 2.2. Fig. 3(a) depicts a thermochemical plume emerging above the inner core boundary, from where a packet of rapid and azimuthally confined QGA waves is emitted. These waves are transverse and therefore best seen on the azimuthal component of velocity acceleration when propagating in the cylindrical radial direction. As it propagates outwards, the wave packet respects the generic behaviour previously described in fig. 9(c) of AG21. Propagation speeds approaching the one-dimensional Alfvén speed $V_A = D/\sqrt{3}\tau_A = 225$ km yr^{-1} are initially observed near the emission point. Consistent with a transition from QGA to QGMC, wave packet slowdown is subsequently observed at mid-depth in the core, with propagation velocities down to about 130 km yr^{-1} at this point, and wave fronts that considerably elongate in the azimuthal direction as a consequence of the dispersive term in eq. (7). We can check that the slowdown, actual velocity and spatial structure are compatible with the dispersion relationship (eq. 7), where we use $k = 2\pi/(500$ km$)$, $H = 2500$ km, $m = 3$ from visual inspection of Figs 3(a) and (b), together with $\Omega = 2\pi/(11.8$ d$)$ from Table 1. As they arrive near the core surface at equatorial position, the elongated wave fronts locally focus near the exit point of radial magnetic flux patches (Aubert & Finlay 2019), causing the magnetic acceleration signals seen in Fig. 2(a). The meridional structure of the waves (Fig. 3b) is highly columnar, as expected from the quasi-geostrophic structuring constraint. The jerk signal from DW events typically results from one wave packet causing multiple rapid alternations in the core surface SA at low latitudes as the successive wave fronts arrive. As mentioned in Aubert & Finlay (2019) and AG21, QGA/QGMC waves are constantly sent outwards from the inner core boundary, but what sets a jerk event apart from this generic behaviour is the strength of the perturbation and a background magnetic field geometry that is suitable for this perturbation to create significant signals at the core surface.

Fig. 4 illustrates the typical dynamic sequence encountered during shallow wave events. Here the event is caused by an ascending buoyancy plume (Fig. 4a) which arrives at shallow equatorial position beneath the core surface. As the toroidal field is locally strong (Fig. 4b), this configuration is prone to instability in the QG-MAC balance, because this non-potential field needs to rapidly decrease as it is pushed towards the mantle where a potential field boundary condition is imposed. Here, the dynamic trigger of hydromagnetic waves emission is the rapid variation in the Lorentz force caused by this rearrangement. The inertial signal in Fig. 4(a) indeed highlights a wave packet confined between the container and a magnetic field line, clearly emitted from the field line tip that is expelled from the core. The wave packet propagates along the magnetic field line, first azimuthally westwards and then downwards as the line bends, before being dispersed. In the azimuthally propagating phase, transverse wave patterns are this time best seen by imaging the cylindrical radial component of flow acceleration. Fig. 4(b) shows that the internal dynamic structure is again highly columnar and confirms quasi-geostrophy as a coherent first order description. Here the magneto-inertial QGA wave nature is further confirmed by a propagation speed very close to the one-dimensional Alfvén speed

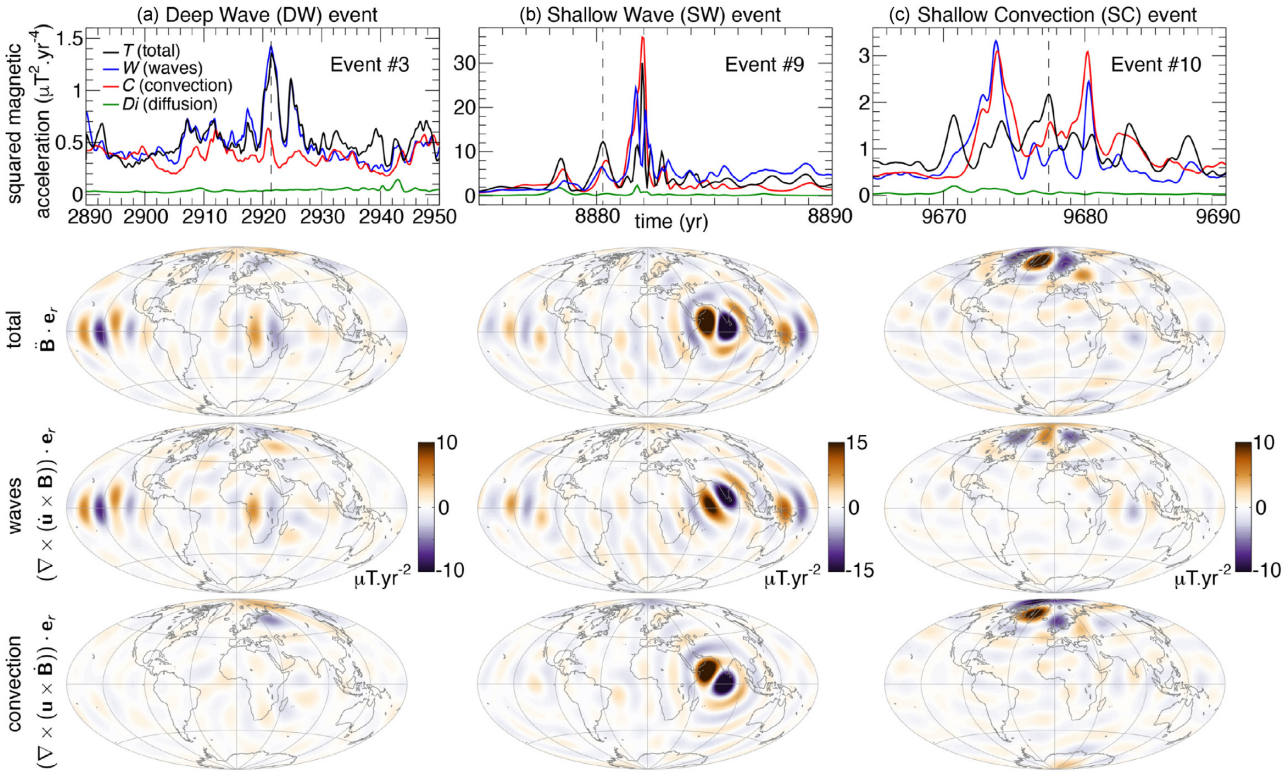

Figure 2. Mean squared values over the core surface of terms contributing to the secular acceleration eq. (17) up to spherical harmonic degree 13, for the three jerk events 3, 9 and 10 (columns a,b,c). Top row: time-series of the total T (black), wave W (blue), convective C (red) and diffusive Di (green) contributions (see text). The vertical dashed lines mark the reference time of the peak in E_{SA} causing the strongest signal in E_J. At this reference time, the next rows successively represent hammer projections of the radial component at the core surface for the total secular acceleration, the wave contribution from the product of $\dot{\mathbf{u}}$ and $\mathbf{B}$, and the convective contribution from the product of $\mathbf{u}$ and $\dot{\mathbf{B}}$.

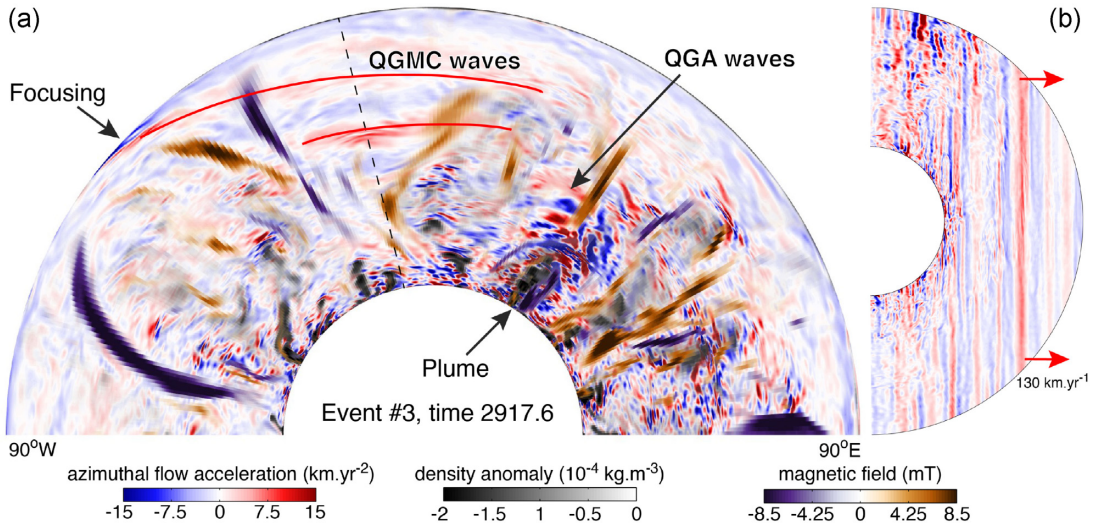

Figure 3. Structure of azimuthal flow acceleration (red/blue), density anomaly (shaded grey) and radial magnetic field (orange/purple) in a portion of the equatorial plane (a) and in a meridional plane (b) located by the dashed line in (a), during the deep wave (DW) event 3, with QGA waves being sent out by a buoyancy release at the inner core boundary (plume). The selected time is shortly before the SA pulse in the event (see Fig. 2a). The red curves in (a) locate the azimuthally elongated QGMC wave fronts.

$D/\sqrt{3}\tau_A = 225$ km yr^{-1}. Neither wave slowdown nor dispersion are observed as long as the wave travels in the azimuthal direction. This indicates that the influence of the Coriolis force is constantly mitigated, presumably because of the small wavelength adopted by the perturbation and the container topography that remains invariant along an azimuth. The SW mechanism locally features strong flow and flow acceleration perturbations, together with strong magnetic field and SV, such that both contributors to eq. (17) lead to

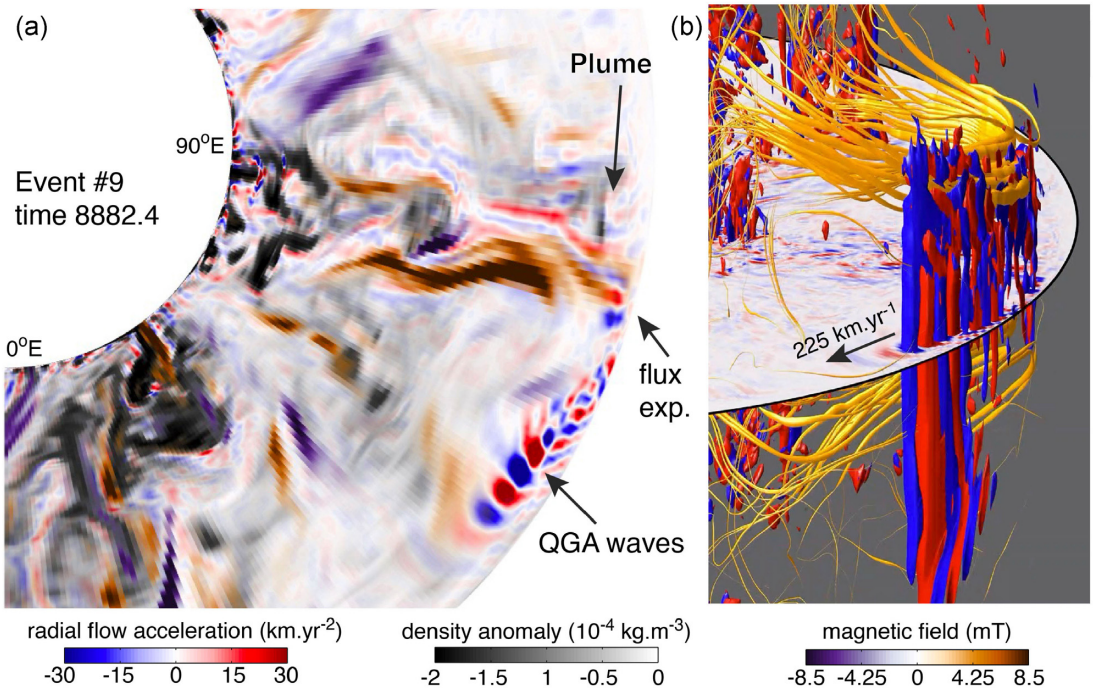

Figure 4. Structure of the cylindrical radial flow acceleration (red/blue), density anomaly (shaded grey) and radial magnetic field (orange/purple) in a portion of the equatorial plane (a) and in a 3-D rendering (b) during the shallow wave (SW) event 9. The selected time is near the maximal SA pulse of the event (Fig. 6c). Here QGA waves are emitted as a shallow convective upwelling pushes magnetic field lines towards the core surface and forces a rapid local rearrangement of field lines. In (b) 3-D magnetic field lines are represented with thickness proportional to the local magnetic energy, and two isosurfaces of cylindrical radial flow acceleration have been represented at levels ± 20 km yr^{-2}.

the strongest magnetic acceleration pulses and jerks seen in the catalogue (see Fig. 2b and diagnostics E_J^{max}, E_J^{max}/E_{SA}^{max} in Table 2).

Shallow wave events systematically occur while a process of expulsion of toroidal field from the core is active. Flux expulsion is a slow kinematic process, and as such it is not responsible for the jerk signals for instance seen in Fig. 2(b)—the hydromagnetic waves that are suddenly emitted as the flux rearranges beneath the core surface are the dynamic explanation here. It is however useful to investigate whether an observable signature in the core surface magnetic field can be associated to SW events. As can be expected, Fig. 5 shows that this signature consists of the appearance of new, oppositely signed pairs of magnetic flux patches at low latitudes. These structures are typically of small scale at native model spatial resolution (Figs 5a and b) and the ones that are expelled during jerk events are only infrequently seen at the typical resolution $\ell \leq 13$ of geomagnetic observations (Figs 5c and d), as attested by the nearly vanishing values of the diagnostic MFS in Table 2 for most jerk events. Only events 1, 6 and 9 (imaged in Fig. 5d) have values of MFS exceeding unity, meaning that the large-scale signature of magnetic flux expulsion during the event clearly deviates from the typical behaviour of the 71p model. Event 2 notably features two equatorial locations where flux expulsion takes place during the event (Fig. 5a), one (beneath India) being located on top of a convective upwelling, and the other one (beneath Central America) on top of a downwelling (where the mechanism described above can be reversed). With MFS $= 0.7$ for this event, the Indian expelled patches are barely visible and the American patches are invisible at large scale.

In both SW and DW types of wave-driven jerk events, we finally note that quasi-geostrophic Rossby waves are also emitted from the QG-MAC disruption points in addition to QGA waves. Consistently with the observations made in AG21, these waves propagate azimuthally eastwards at speeds in excess of 1000 km yr^{-1}. This is a second natural by-product of inertial compensation to leading-order force balance disruptions, that is irrelevant to the production of jerk signals as the QG Rossby waves carry much less magnetic than kinetic energy (e.g. Gerick *et al.* 2021).

3.3 Spatio-temporal magnetic signatures of wave-driven events

Fig. 6 presents close-ups of the SA and jerk energies E_{SA} and E_J (eqs 8 and 9) in the vicinity of four jerk events. Shallow wave events (e.g. events 2 and 9 depicted in Figs 6a and c, and events 1, 6 and 12) frequently have long temporal baselines up to 60 yr (see 'Duration' diagnostic in Table 2), as they unfold over a multidecadal duration linked to the convective and magnetic evolution of the system near the core surface. This creates a multiplicity of chaotic occurrences where the QG-MAC balance is disrupted and hydromagnetic waves causing the jerk signals are emitted. As previously mentioned, these events tend to produce the strongest jerks of the database in terms of the SA energy E_{SA}. The peaks in E_{SA} can be too sharp to be fully detectable once a 3-yr moving average is applied to compute E_J (Figs 6a and c). This results in E_J^{max}/E_{SA}^{max} well below unity, with values as low as 0.1 being for instance observed in event 6 (Table 2). SW events of shorter duration (e.g. events 5c, 7, 11 and 13 shown in Fig. 6d) only feature one instance of wave emission. In contrast with SW events, deep wave events (events 3, 5a, 14 and 4 imaged in Fig. 6b) show a significantly more regular alternation of peaks in E_{SA}, with corresponding peaks in E_J that are out of phase. Here the successive SA pulses can indeed be seen as belonging to the same

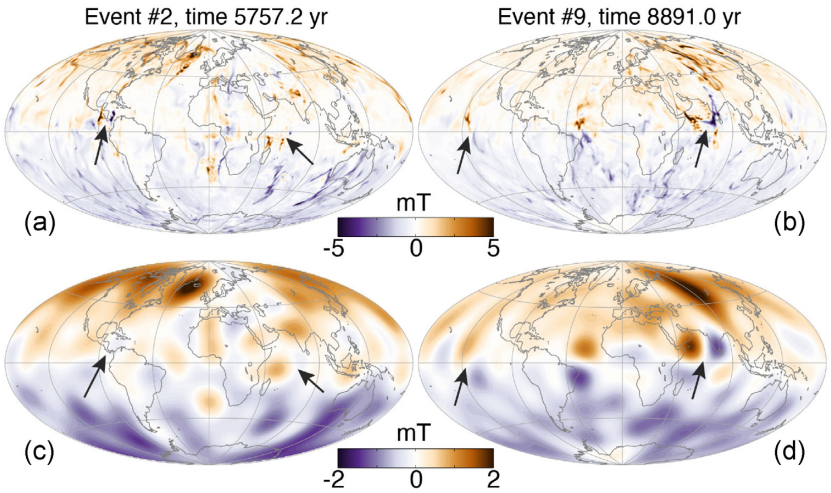

Figure 5. Hammer projections of the CMB radial magnetic field during jerk events 2 (a,c) and 9 (b,d). In (a,b) the field is presented at native model spatial resolution, and is truncated at spherical harmonic degree 13 in (c,d). Black arrows locate the magnetic flux structures that are expelled as these events occur.

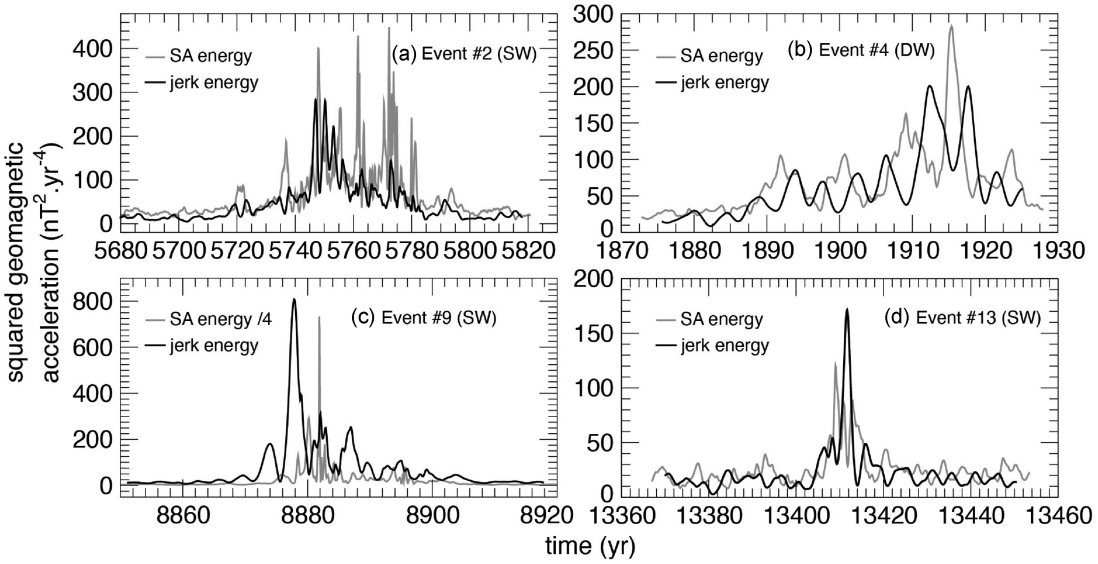

Figure 6. Time-series of the jerk energy E_J (black) and the SA energy E_{SA} (grey) during the three shallow wave (SW) events 2,9,13 (a,c,d) and the deep wave (DW) event 4 (b).

wave packet caused by a single deep convective trigger, explaining their regularity and alternation. The duration of the event is also shorter (up to 30 yr) because the packet life time is limited by the duration of the trigger and by dispersion (see Fig. 3 and Section 2.2). Deep wave events typically feature lower SA energies than shallow wave events, but at the same time they achieve ratios E_J^{max}/E_{SA}^{max} closer to unity because of the regularity of the signal.

The spatio-temporal characteristics of the simulated jerk events are best explored by looking at time-longitude plots of radial SA at the equator of the core surface (Fig. 7). Compared to similar plots in Aubert & Finlay (2019), it is immediately apparent that the evolution from the Midpath (50 per cent of path) to the 71p model leads to alternating SA pulses that are now significantly clearer, stronger and shorter. This is because the Alfvén time has been shortened by roughly a factor 2.5 relatively to the magnetic diffusion time. This also commonly produces more polarity alternations in these SA pulses within the duration of a given wave packet [diagnostic 'Multi (time)' in Table 2], most clearly seen in deep wave, single trigger events such as event 4 (Fig. 7a). With a single deep trigger also, SA polarity changes tend to synchronize across longitudinally remote locations, as a consequence of the long azimuthal wavelength of arriving QGMC wave fronts (see Figs 3a and 9a). These alternating and synchronized signals are still decently resolved in Fig. 7(b), where we simulate the commonly accessible resolution for SA in satellite geomagnetic field models by filtering Fig. 7(a) down to spherical harmonic degree 9 and applying a 3-yr moving average in time.

Examining the more complex event 5 that involves several different triggers (Fig. 7c) reveals a number of notable differences with the above description. The multiplicity of triggers is first attested by the unsynchronized longitudes and times at which the subevents occur, as well as the absence of temporal coherence along a given longitude (note that event 5b is not present on this equatorial view as it is a high-latitude event). The shallow wave event 5c furthermore involves a typical 'cross-over' signature (from the denomination introduced by Hammer & Finlay 2019) where two intense adjacent

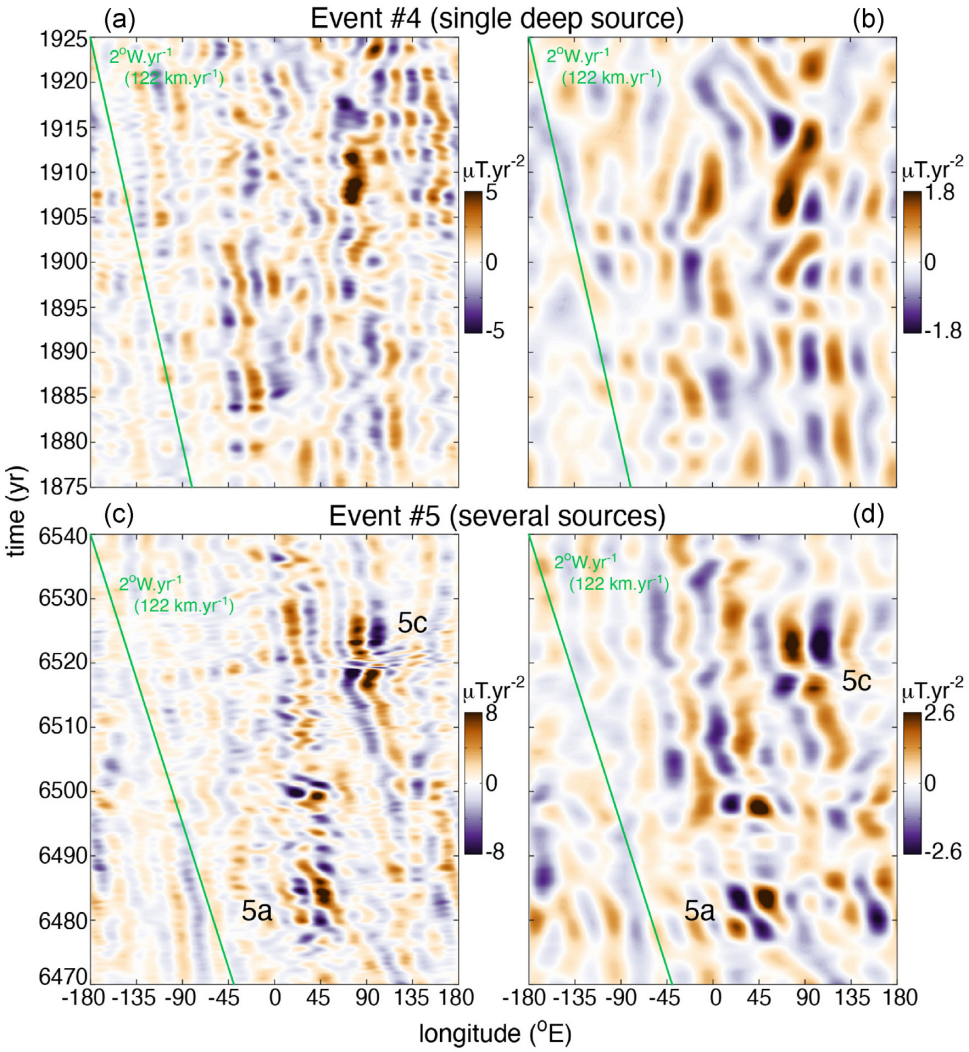

Figure 7. Time-longitude plots of equatorial, radial SA at the core surface for jerk events 4 (a,b) and 5 (c,d). SA is truncated at spherical harmonic degree 13 and presented at native temporal resolution in (a,c). In (b,d), SA is truncated at degree 9 and a running average in time with window width 3 yr is applied, to reflect the commonly accessible spatio-temporal resolution of SA in satellite-based geomagnetic field models. For reference, the slanted green lines represent a westward drift at a rate of 2 degrees per year (122 km yr^{-1} at the core surface).

SA patches rapidly switch their polarity within less than a year. This signature is typical of rapid patch alternation and rotation found in SW events (see also Fig. 2b). These extremely short timescales are filtered out once the spatio-temporal resolution degradation step is performed (Fig. 7d), with the filtered view still showing the 'cross-over' but with a timescale of about 3 yr that is no longer representative of the rapidity of the event.

When examining filtered time-longitude plots (e.g. Figs 7b, d and 8), about half of the analysed jerk events feature evidence of azimuthal drift of core surface SA structures at speeds in excess of 100 km yr^{-1}, significantly exceeding that of the convective westward drift (about 15 km yr^{-1}). However, the azimuthal drift on such filtered plots should be examined with some caution, as the drift can be much less obvious when looking at higher resolution plots (Figs 7a and c). For instance, an apparent eastward drift in the positive flux patch around time 1910 in event 4 (Fig. 7b) becomes spurious when looking at Fig. 7(a). Likewise, the 'cross-over' event 5c shown in Fig. 7(c) appears as a westward-drifting positive patch in Fig. 7(d). As the secular acceleration spectrum is blue, the addition of small scales in the time-longitude diagrams can indeed significantly modify the result, such that a clear physical connection between the drift of the large-scale SA patches and an underlying physical mechanism cannot be guaranteed. Despite these limitations, westward propagation can still be coherently observed over 10–15 yr in several events (diagnostic 'Drift' in Table 2, Fig. 8). Among the possible candidates to explain such drifts, Alfvén wave propagation such as observed in event 9 (Fig. 4) occurs preferentially westwards, because of the field line asymmetry promoted at the top of the core by the anticyclonic vortices supporting the westward-drifting general circulation (see e.g. fig. 8 of Aubert 2019). QGMC waves also feature an azimuthally westward phase velocity at the core surface (Gerick *et al.* 2021; Gillet *et al.* 2022b).

The deep wave event 4 illustrates the long-range longitudinal synchronization that can arise because of the spatial structure of hydromagnetic waves involved in jerks (as reported by the diagnostic 'Region' in Table 2). The regular arrival of successive azimuthally elongated fronts from the QGMC wave packet (Fig. 9a) sets a common pace for the low-latitude alternation of remote SA patches at the core surface (Fig. 9b). This is best seen here in the Indian and Atlantic regions, where low-latitude radial magnetic flux patches

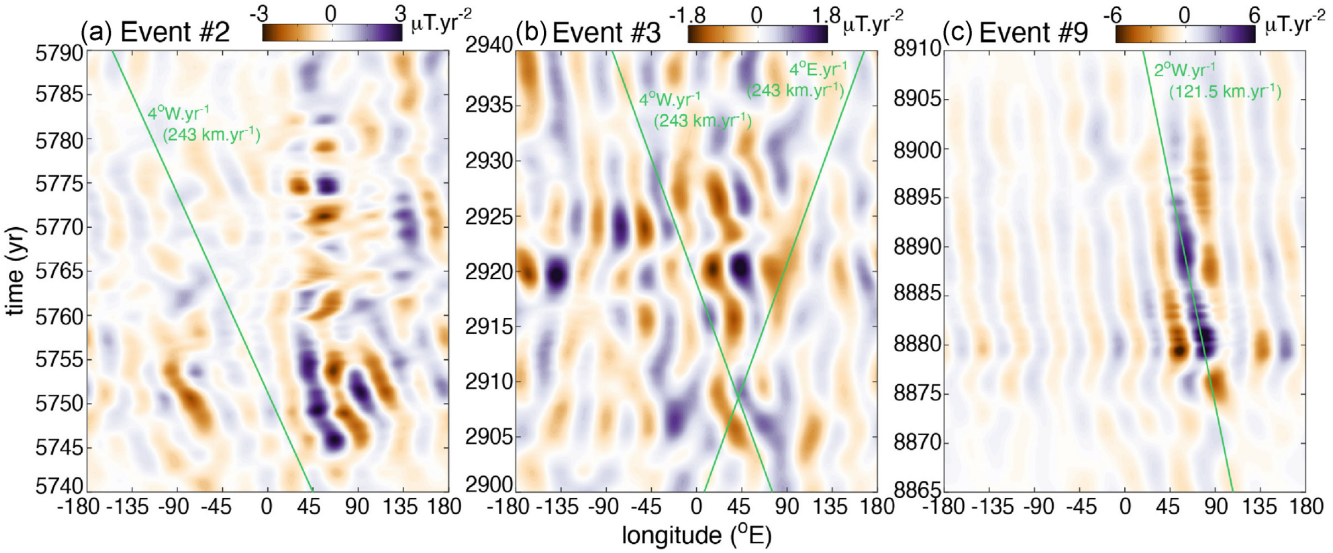

Figure 8. Time-longitude plots of equatorial, radial SA at the CMB for jerk events 2 (a), 3 (b) and 9 (c). SA is truncated at degree 9 and a running average in time with window width 3 yr is applied. Green lines delineate east- and westward propagation at the reported angular and linear velocities.

are found during this event, as a consequence of the general circulation pattern in the model (Aubert *et al.* 2013). At the Earth surface (Fig. 9c) the jerk event therefore comprises several longitudinally remote, large-scale SA patches that alternate their polarity in time in a collective manner, either by pulsating in place or by rotating around their focal point. We also note that the slanted structures of QGMC waves at the core surface (Fig. 9a) reflect an axially invariant and azimuthally spiralled deeper structure (Fig. 3a) that is characteristic of such waves (Gillet *et al.* 2022b).

3.4 V-shaped secular variation patterns during jerks

The presence and geographical distribution of 'V-shapes' in time-series of individual East SV components at Earth surface is analysed in Fig. 10. A qualitative visual inspection confirms that the local value of $\chi(\theta, \varphi)$ (eq. 15, detection method 1 in Section 2.3.3) that serves to colour-code the SV traces here assesses fairly well the sharpness of changes in decadal trends, independent of the background magnitude of SV and SA. A threshold value $\chi(\theta, \varphi) > 3$ appears suitable to assess the 'Globality' of jerk events (Table 2). Strong shallow wave jerks like events 1 and 9 (Figs 10a and d) and also events 2 and 6 produce clear, detectable V-shapes (blue traces) that are generally widespread around the globe, with 'Globality' up to 66 percent in the case of event 9. The weaker deep wave jerk events are typically only regional, with 'Globality' up to about 40 percent. At most locations, the tips of V-shapes are generally approximately synchronized with the global occurrence times t_i (red dots) extracted from eq. (12), with possible delays in the arrival of the waves at different longitudinal sectors at low latitudes not exceeding a couple of years. In the case of local delays with respect to t_i, $\chi(\theta, \varphi)$ is reduced by construction, such that this quantity also partly assesses the synchronicity of V-shapes. Jerks with multiple SA pulses in time present multiple V-shapes, that occur as a succession of V- and inverted V-shapes, as expected from the polarity changes of the SA (see e.g. Fig 9c). Interestingly, it is not needed to have a jerk source at high latitude at the core surface (like jerk 8, Fig. 10c) to observe V-shapes at high latitudes at Earth surface. For instance, events 1 and 9 with a jerk source in the equatorial Asian region produce discernable V-shapes in Europe. The distance between core surface and Earth surface, together with the properties of mathematical upward continuation of the potential field, suffice to distribute the perturbation over a wide region of the Earth surface (see insets in Fig. 10). The creation of widespread and nearly synchronized V-shapes across different field components is therefore simply a geometrical result. Despite this extent, none of the simulated jerks are labelled as truly global, according to our definition of 'Globality', and the regions of detection (blue traces in Fig. 10, blue regions in Fig. 12) are frequently reminiscent of how jerk sources are localized at the core surface, both in longitude and latitude (compare Fig. 12 with insets in Fig. 10). We note that even observed geomagnetic jerk events regarded as worldwide, such as the 1969 and 1978 events, are also not detected at all locations (Brown *et al.* 2013).

Because the field outside the core is potential, the global occurrence time t_i of a jerk is the same if the azimuthal field component is replaced by the radial or meridional component in eq. (12). An examination of V-shapes on other directions of the SV than east (e.g. the downward component, Fig. 11) confirms this synchronization of jerks across components at the global level. At the local level, however, different components have different sensitivities to the evolving field at the core–mantle boundary (e.g Gubbins & Roberts 1983), such that jerk events are not necessarily seen in all components at a specific location (compare the SV traces of Figs 10 and 11, e.g. beneath the Americas). Temporal V-shape delays of a few years between components at the same location are also possible (see e.g. beneath central Australia), similar to the above mentioned regional delays within one component. For all events in the catalogue, downward SA changes are about twice stronger, but also more focused laterally than in the other directions (compare the insets of Figs 10 and 11). This is a geometrical effect that stems from the local dipolar nature of the radial SA perturbations at the core surface (Fig. 2), and, again, the potential nature of the field outside the core. Despite the higher amplitude, the stronger focusing results in a less widespread detectability on this component (51 per cent versus 66 per cent on the east component for jerk 9). On average over the entire catalogue, the east component therefore still features the most widespread detectability at Earth's surface, with Globality

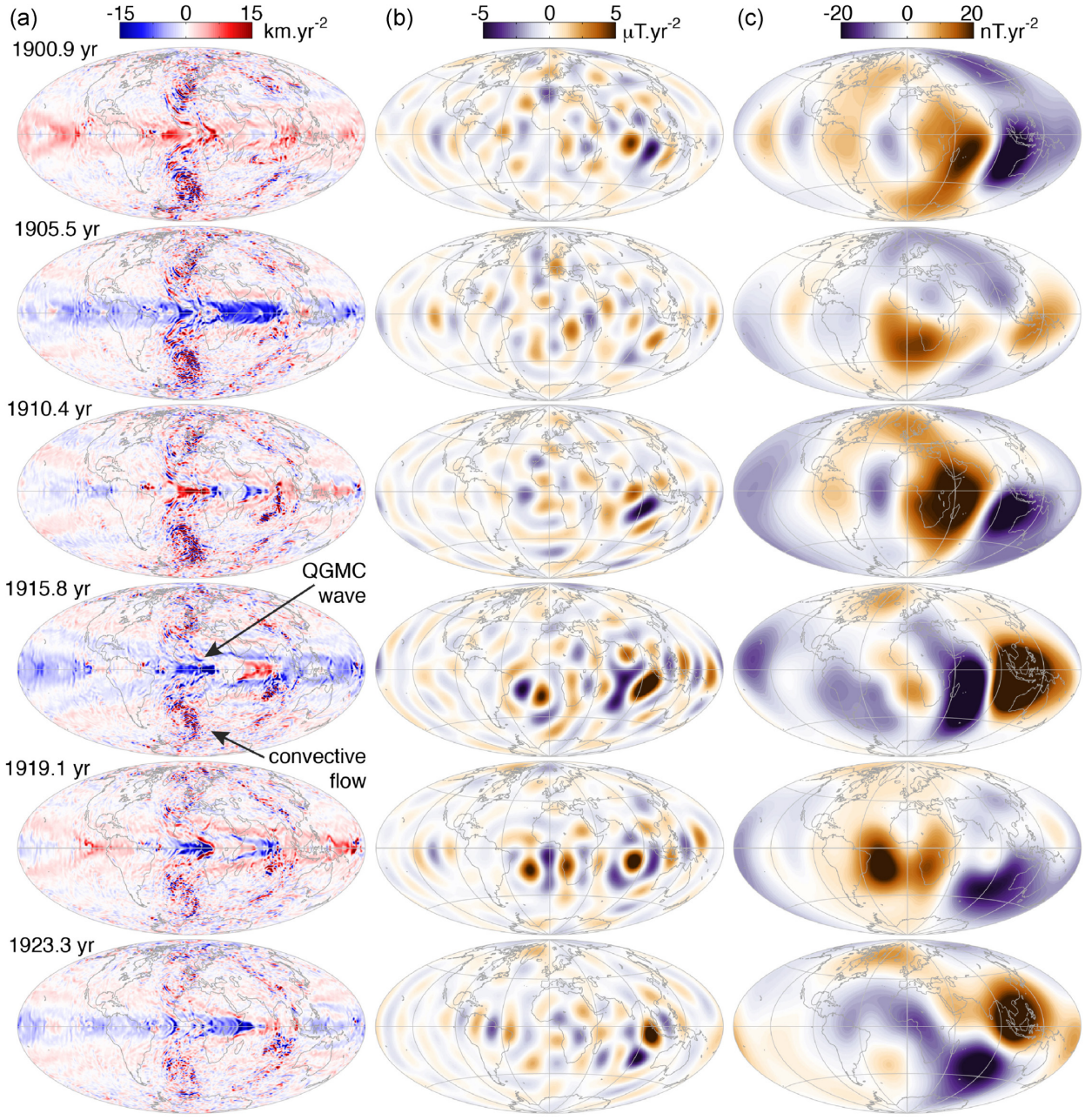

Figure 9. Temporal sequence of flow and magnetic patterns during jerk event 4. Hammer projections of: (a) azimuthal core surface flow acceleration, (b) core surface radial SA truncated at spherical harmonic degree 13 and (c) Earth surface radial SA.

ratings according to $\chi > 3$ being 1.2 and 1.3 times higher than with similar criteria constructed for the downward and north components, respectively. Fig. 12 finally assesses the detectability of V-shapes in a case where the secular acceleration is not globally known, as is the case when only observatory data are available. When compared to method 1 (Section 2.3.3), which assumes global knowledge of the SA, the results from method 2, which is tailored to the observatory data case and intrinsically assumes piecewise linear behaviours, as expected yield a more contrasted and restrictive image of what is considered a jerk event. Jerks detected at locations found by method 1 are nevertheless often retrieved by method 2, with the notable exception of the weaker jerk 3.

3.5 Other signatures of jerk events

Significant surges in the SV amplitude A_{SV} at Earth surface (diagnostic SVS in Table 2 at or above unity) are observed during five simulated jerk events of the catalogue (four instances of which are imaged in Figs 13a–d). For the strong, shallow wave events 1, 6, 9 (Figs 13a, c and d) that occur during visible core surface magnetic flux expulsion at large scale, it is natural to also observe surges in the Earth surface SV energy, with the corresponding signature at the core surface comprising the appearance of strong patches of SV as the flux is expelled, corresponding to intense temporal variations of the SV at some locations (Figs 10a and d). SV surges can however also simply result from hydromagnetic wave dynamics, as seen for

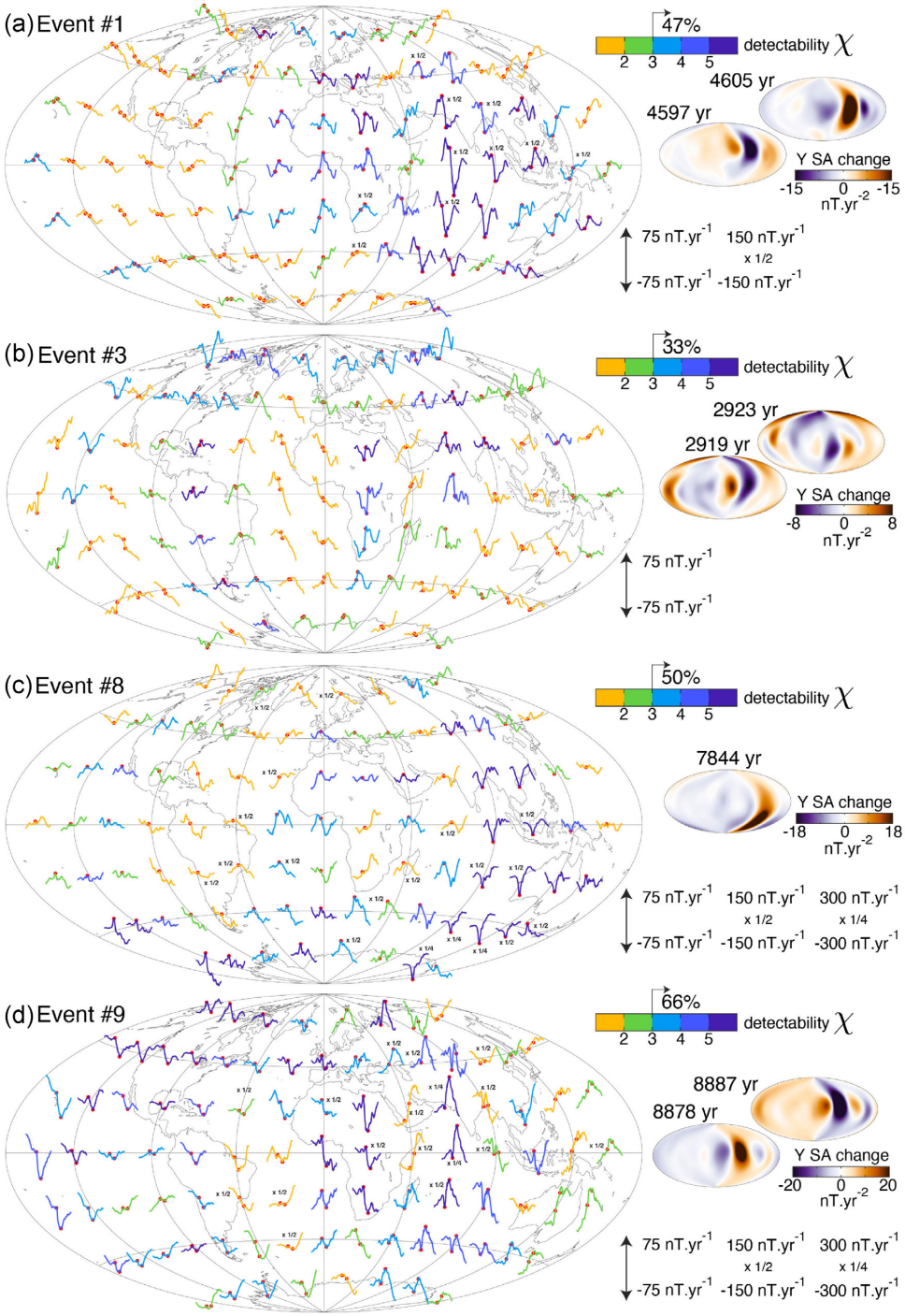

Figure 10. Time-series of the east component of the SV (or Y, along $\mathbf{e}_\varphi$, with average being removed), presented over 50 yr at regularly spaced locations of the Earth surface, during the low-latitude shallow wave events 1, 9 (a,d), the low-latitude deep wave event 3 (b), and the high-latitude, surface convection event 8 (c). Red dots locate the tips of 'V-shapes' at the maxima t_i of $\Delta SA_\varphi(t)$ (eq. 12), with correspondings maps of the smoothed SA changes $J_\varphi(\theta, \varphi)$ (eq. 13) imaged in the insets. SV traces are colour-coded according to the local value of the detectability diagnostic $\chi(\theta, \varphi)$ (method 1, eq. 15). The 'Globality' (Table 2) or fraction of Earth surface over which $\chi > 3$ is also reported.

instance during the deep wave event 4 (Fig. 13b). Flow perturbations carried by the hydromagnetic waves are nominally of smaller amplitude than the background convective flow, such that the wave signatures are more easily highlighted in flow accelerations rather than in the flows themselves (AG21). However, as the wave patterns concentrate at equatorial positions, the wave-driven flows can become locally and temporarily as strong as the background flow (Fig. 13e) while maintaining a large-scale azimuthal structure, such that they can have an impact on the Earth-surface SV (Fig. 13f), in addition to their acceleration having an impact on the SA (as previously illustrated in Fig. 9).

We finally analyse in Fig. 14 the length-of-day signature of jerk events produced in the simulation. Only the three strongest shallow wave jerks 6, 9 and 12 have been found to create distinct inflexions

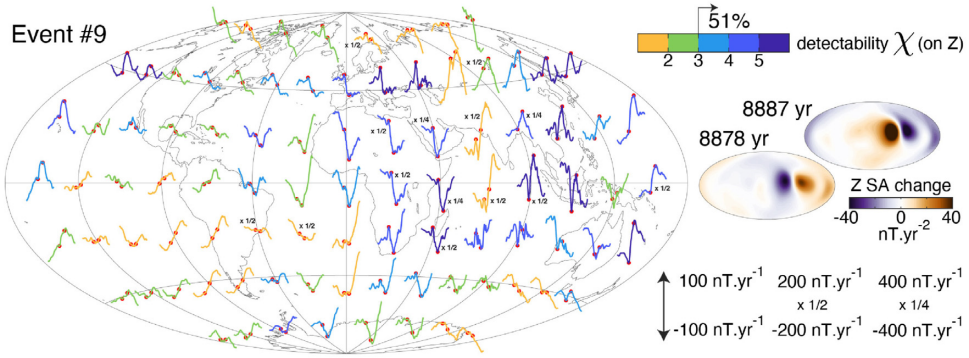

Figure 11. Same as Fig. 10, for time-series of the downward component (or Z, along $-\mathbf{e}_r$) of SV during jerk event 9. The downward component is also used in place of the east component in eqs (13) and (15) to compute the smoothed SA change maps in the insets and local detectability $\chi(\theta, \varphi)$.

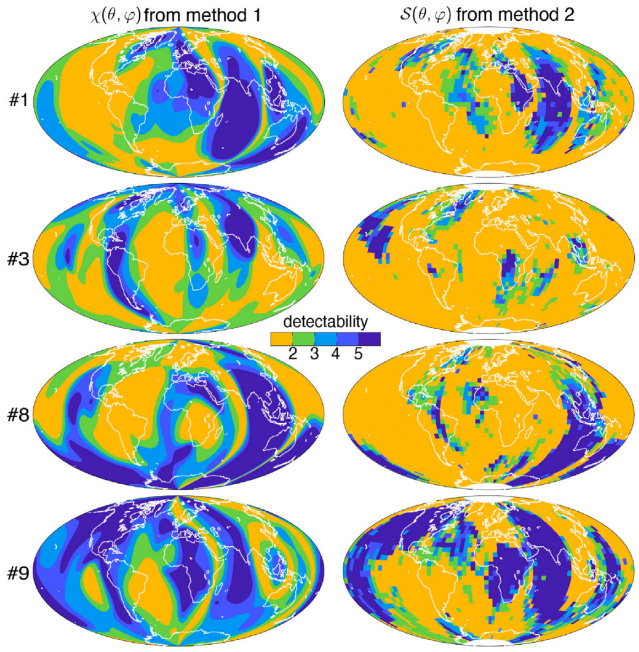

Figure 12. Hammer projections of the detectability criteria $\chi(\theta, \varphi)$ (method 1, eq. 15) and $\mathcal{S}(\theta, \varphi)$ (method 2, eq. 16), both computed for the East component of SV at Earth's surface for jerk events 1, 3, 8 and 9 imaged in Fig. 10. See Section 2.3.3 for details on the methods.

in d(LOD)/dt that can be clearly associated to the jerk-driven acceleration of the CMB magnetic torque $\mathrm{d}^2\Gamma_\mathrm{M}/\mathrm{d}t^2$ (see eq. 5). The spikes in $\mathrm{d}^2\Gamma_\mathrm{M}/\mathrm{d}t^2$ help to locate these inflexions in time-series of d(LOD)/dt (red regions in Fig. 14), but we note that these time-series also present a significant granularity away from inflexions related to jerks, that relates to accelerations $\mathrm{d}^2\Gamma_\mathrm{G}/\mathrm{d}t^2$ in the gravitational torque exerted on the mantle by the inner core. With $\Gamma\tau/\rho D^5\Omega = 0.75$ in the 71p model, $I_M = 7.1\ 10^{37}$ kg.m^2 (Ahrens 1995), and the previously used values of D and ρ (see Table 1), the gravitational restoring time $I_\mathrm{M}/\Gamma\tau$ amounts to about 23 numerical days of length $2\pi\tau_\Omega = 11.8$ d, or 0.74 yr, in this case indeed in the same range as jerk-induced perturbations in the length-of-day. It appears therefore that both the relative strength and timescales of gravitational and magnetic torques are crucial to the isolation of jerk signatures in the length-of-day time-series.

4 DISCUSSION

4.1 A common origin for most simulated jerks

The analysis of the catalogue has confirmed that most simulated jerks originate from a common physical root cause, that is the emission of QG magneto-inertial waves (Figs 3 and 4) following a disruption in the leading-order QG-MAC force balance (Fig. 2). The results from the 71p model therefore broadly support the initial proposal of Aubert & Finlay (2019) regarding the origin of geomagnetic jerks. The timescale separation (Table 1) between the convective overturn time τ_U representative of inertia-less QG-MAC evolution, and the interannual Alfvén time τ_A, characteristic of inertia-bearing Alfvén wave propagation (with possible subsequent evolution as QGMC waves at a similar timescale), is key to a clear temporal isolation of jerk signals from the background convective dynamo. As this separation has increased from the Midpath model of Aubert & Finlay (2019) to the 71p model used here (Table 1), these signals are now significantly clearer (e.g. Figs 6, 7 and 9), and, as we shall see below, also closer to geomagnetic observations. This modelling success is supportive of the QG-MAC path theory (Aubert *et al.* 2017), the associated amplitude hierarchy of force balances in the core (Schwaiger *et al.* 2019), and of the estimate $\tau_A \approx 2$ yr made for Earth's core by Gillet *et al.* (2010). The condition $\tau_A \gg \tau_\Omega$ requires that the waves evolve under a strong rotational constraint. Being non-axisymmetric, this means that they evolve in a quasi-geostrophic equilibrium (Section 2.2), and present axially invariant wave fronts. Aside from these wave-driven jerks, a minority of events have been found to only involve the background convection. It is possible that these could be more frequent in other setups than that adopted in the 71p model, for instance if the core surface is made convectively unstable instead of being neutrally buoyant. This latter possibility is however not currently favoured because of constraints on the core–mantle boundary heat flow and the expected high value of the core thermal conductivity (Davies *et al.* 2015; Frost *et al.* 2022). The presence of strong stratification at the core surface also tends to hinder wave-driven jerks (Aubert & Finlay 2019), suggesting that a scenario close to neutral buoyancy near the core surface may be most plausible.

Wave-driven simulated jerks have been classified here according to whether these waves originate deep in the core (Fig. 3), as initially reported by Aubert & Finlay (2019), or close to the core surface (Fig. 4), as reported here for the first time. Waves originating close to the core surface typically produce stronger jerk signals (Fig. 6, Table 2), and due to their amplitude are associated to clearer signatures

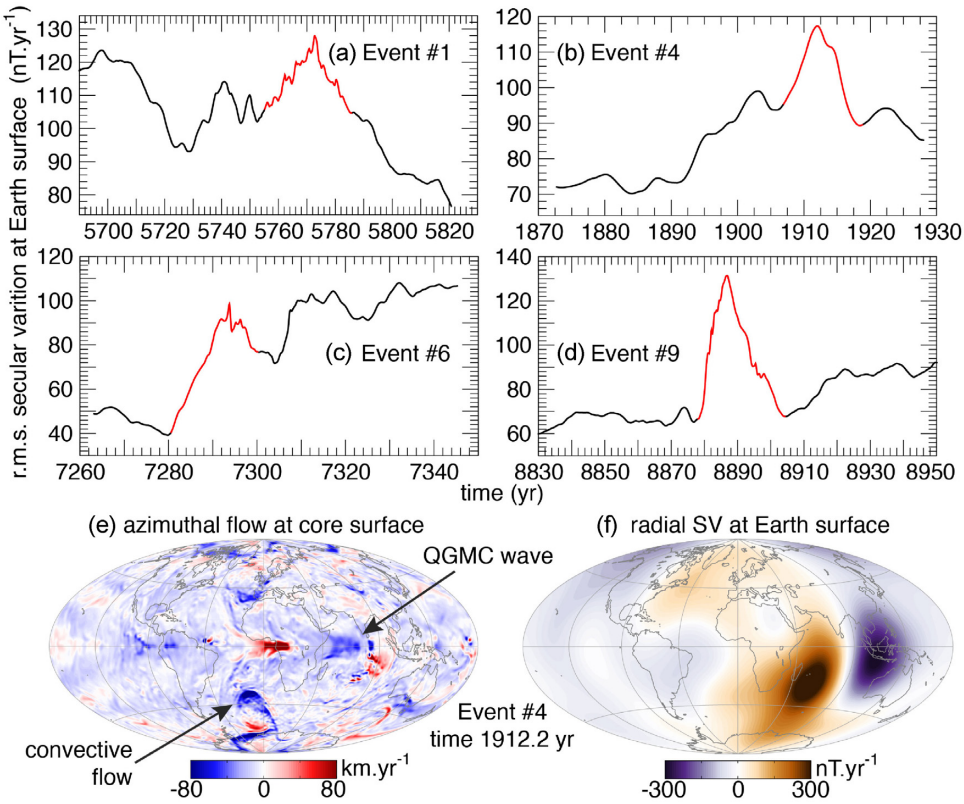

Figure 13. Top panel: time-series of the Earth surface r.m.s. SV amplitude A_{SV}, during events 1 (a), 4 (b), 6 (c) and 9(d). The red portions of the curves delineate the surges occurring during the jerk events. Bottom panel: hammer projections of the core surface azimuthal flow (e) and Earth surface radial component of SV (f) during the surge of event 4.

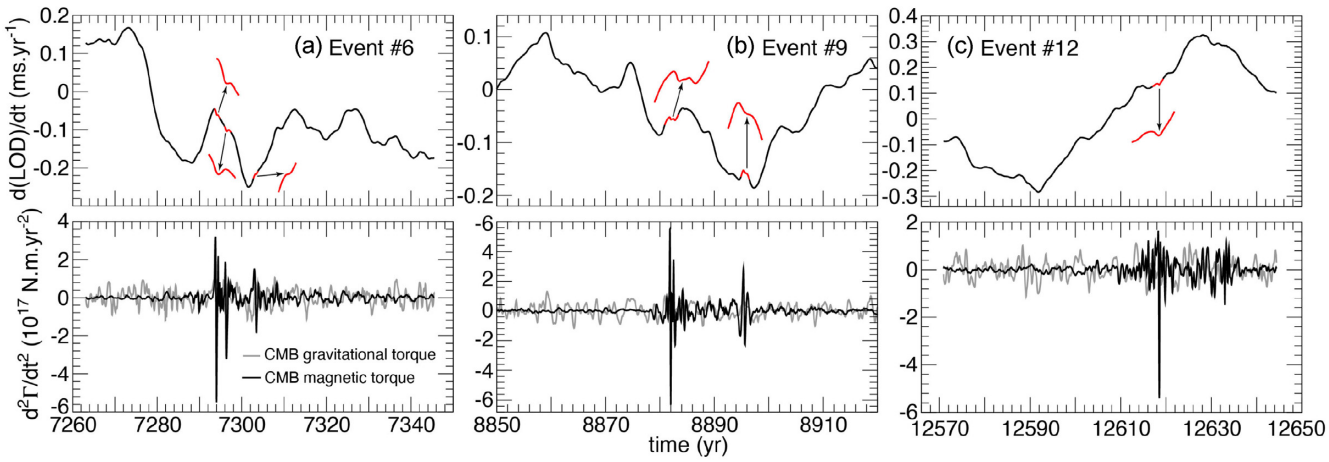

Figure 14. Top row: time-series of the length-of-day rate of change d(LOD)/dt in the vicinity of jerk events 6 (a), 9 (b) and 12 (c). Bottom row: corresponding time-series of the accelerations $d^2\Gamma_M/dt^2$ and $d^2\Gamma_G/dt^2$ of the magnetic and gravitational torques, showing magnetic torque perturbations caused by jerks that significantly exceed those of the gravitational torque. The corresponding inflexions in d(LOD)/dt (see eq. 5) are highlighted in red and magnified in the top row.

than deep triggered waves. These points have admittedly biased our handpicking process, such that the catalogue includes more near surface triggered waves than deep triggered wave events (9 versus 4). Still, it should be kept in mind that deep waves are constantly sent out by convective plumes attached to the inner core (AG21), while such plumes only occasionally occur closer to the core surface, where they can reorganize the magnetic flux and trigger shallow waves. Deep triggered wave jerks are therefore intrinsically more frequent, with many small-amplitude events forming the baseline of the secular acceleration and jerk energy time-series in Fig. 1. A detailed analysis of all these smaller events is at present difficult because of the challenges still involved in separating waves of small amplitude from the background convective signals, and because of the larger number of events. Consistent with the hypothesis of ubiquitous deep wave arrivals, QGMC waves have recently been regularly detected in the geomagnetic record of the past 20 yr (Gillet *et al.* 2022b). Our analysis (Fig. 3) has clarified how quasi-geostrophic Alfvén wave packets initially emitted by deep convective perturbations turn into

QGMC waves with long azimuthal wavelengths as they ascend in the outer core.

4.2 Simulated versus observed geomagnetic jerks

Our analysis of deep-triggered wave jerks is based on a detailed spatio-temporal knowledge of secular acceleration at the Earth and core surfaces. This is available from geomagnetic field models combining satellite and ground observatory data, and covering the past 20 yr (e.g. Finlay *et al.* 2020; Hammer *et al.* 2021). The geomagnetic field model CHAOS-7.8 (Finlay *et al.* 2020) yields jerk energies $E_J = 106$, 84, 141 and 127 $\mathrm{nT^2\,yr^{-4}}$ for the 2007, 2011, 2014 and 2017 jerks. The deep-triggered wave events of the catalogue (Table 2) reach similar typical jerk energies $E_J = 100 - 200$ $\mathrm{nT^2\,yr^{-4}}$. Time-series of E_J and E_{SA} furthermore present multiple coherent alternations and respective phase shifts (Fig. 6b) in better agreement with their geomagnetic counterparts than the results previously obtained with the Midpath model (see fig. 1 in Aubert & Finlay 2019). The success of these events in reproducing the properties of recent geomagnetic jerks is perhaps best illustrated by equatorial time-longitude plots of core surface radial secular acceleration (Figs 7b and 8b) and their equivalents from satellite geomagnetic field models in the epoch range 2000–present (e.g. Chulliat *et al.* 2015; Aubert & Finlay 2019). In the model, the arrival of a deep-triggered wave train at low latitudes at the core surface reproduces the observed rapid and multiple alternations of longitudinally localized, intense, low-latitude secular acceleration patches. While the previous Midpath model lacked multiple alternations, and featured a discrepancy in timescale compared to geomagnetic observations (see fig. 2 in Aubert & Finlay 2019), these two features are now better captured by the 71p model output. Following a decrease of the Alfvén time from $\tau_A = 14.3$ yr in the Midpath model to $\tau_A = 5.8$ yr in the 71p model, the observed typical periods are more in line with the geomagnetic data. The analysis of geomagnetic time-longitude plots has revealed a long-range azimuthal communication between foci of equatorial secular acceleration (e.g. Chulliat *et al.* 2015) that is also reproduced in a clearer manner by the 71p model output. Events with a common origin but occurring at distant locations are a result of azimuthally elongated hydromagnetic wave fronts (Fig. 9). At the Earth's surface, the jerk secular acceleration signals consist of the appearance of pairs of oppositely signed and rapidly alternating patches (Figs 9c), with large typical length scales of 10^4 km (spherical harmonic degrees 4–6), and typical amplitude up to a few tens of $\mathrm{nT\,yr^{-2}}$ on single components. These patterns agree well with those found in satellite geomagnetic field models, for instance in the vicinity of the 2007 jerk (fig. 1 in Aubert & Finlay 2019), and more recently for the 2017 jerk (fig. 16 in Finlay *et al.* 2020).

Temporal filtering (a running average over a 3-yr window) has been applied to the 71p model output to produce the presented time-longitude plots (Figs 7b, d and 8) and to compute the jerk energy (eq. 9, Figs 1b and 6). This was done in order to bring the secular acceleration to a level of temporal resolution that is easily accessible to modern geomagnetic field models, where a similar filtering step is also useful to their analysis (e.g. Finlay *et al.* 2020). The alternation of deep-triggered wave jerk signals at a timescale commensurate with $\tau_A = 5.8$ yr is not dramatically affected by this filtering (Figs 7a and b), but it can be expected that the same representation of geomagnetic jerks with $\tau_A \approx 2$ yr will be band-limited if the temporal resolution is limited to 3 yr. Some recent geomagnetic modelling approaches use local averaging kernels to image the secular acceleration from satellite data directly at the core–mantle boundary, without resorting to classical spectral and regularization techniques (Hammer & Finlay 2019; Hammer *et al.* 2021). These are able to lower the temporal resolution limit to about a year, and highlight additional interesting features also seen in the events of the catalogue. A 'cross-over' secular acceleration pattern has for instance been reported in 2007 by Hammer & Finlay (2019) at longitude 25°W on the equator (their fig. 10), similar to that seen for the deep wave event 5a in Figs 7(c) and (d), and more clearly for the shallow wave event 5c. Such patterns arise in the 71p model from rapid and synchronous polarity exchange of adjacent secular acceleration patches, following the wave arrival. The 71p model highlights extremely rapid field acceleration cross-overs that indeed require a fine-grained temporal resolution for imaging. Geomagnetic maps of higher temporal resolution also better image the remarkable synchronicity of long range azimuthal correlations in the secular acceleration signals (e.g. epoch 2014, fig. 9 in Hammer *et al.* 2021), that is also found in the time-longitude plots of deep wave events (Figs 7a, b and 8b).

Spatial filtering has also been systematically applied in order to present the core surface secular acceleration from the 71p model. This consists in a truncation at spherical harmonic degree 9 or 13 (see legends in Figs 7–9). While this is not at first glance desirable, it is needed in order to compare the model output to the observed accelerations from geomagnetic field models. It is furthermore necessary because the spectrum of the secular acceleration is blue at the core surface, and hence very difficult to interpret at native resolution. The spatio-temporally filtered time-longitude plots show evidence of structures rapidly drifting east and preferentially westwards at speeds in excess of 100 $\mathrm{km\,yr^{-1}}$ (Figs 7b, d and 8). Such longitudinal drifts have been reported in several analyses of geomagnetic field models, with varying, but generally remarkably high velocities (Chulliat *et al.* 2015; Chi-Durán *et al.* 2020; Gillet *et al.* 2022a). Filtering at two different levels of spatio-temporal resolution however shows that drifts observed on coarse images are not necessarily preserved on finer representations (Fig. 7); the interpretation of such drifts is not straightforward. In connection with the waves creating the jerk signals, possible physical origins for rapid drifts include quasi-geostrophic Alfvén waves propagating westwards along magnetic field lines near the core surface (Fig. 4) or westward phase propagation of quasi-geostrophic magneto-Coriolis waves (Gerick *et al.* 2021). Rossby waves also rapidly propagate in the eastward direction but these are unlikely to be associated with significant magnetic signals, because of their low magnetic to kinetic energy ratio (Gerick *et al.* 2021, AG21).

The signatures of rapid wave signals on flows in the interior of the core (Figs 3 and 4) or at the surface (Figs 9a) are best seen by examining the flow acceleration, where the slowly varying convective contributions are mitigated (AG21), or by bandpass filtering to isolate decadal to interannual periods (e.g. Gillet *et al.* 2019, 2022b). Wave flow convergence at low latitude can also lead to prominent signatures, without the need to remove these contributions (Fig. 13e). In any case, non-axisymmetric signals largely dominate the signatures of axisymmetric torsional waves, such that these can be ruled out as an explanation for the simulated jerks (Aubert 2018). Accounting for recent geomagnetic jerks in terms of accelerating core surface flows also unambiguously requires non-axisymmetric components (Wardinski *et al.* 2008; Silva & Hulot 2012; Kloss & Finlay 2019). The hydrodynamic wave signatures associated with recent geomagnetic jerks at the core surface consist of rapidly alternating flows with several foci corresponding to the localization of intense secular acceleration patches (Kloss & Finlay 2019), in good agreement with those seen during jerk events in the catalogue

(Figs 9 and 13e), both in morphology and typical amplitudes. The preferentially longitudinal flow orientation agrees with the structure of radially propagating, transverse QGMC waves (Gillet *et al.* 2022b), such as those involved in deep-triggered wave events.

Secular variation time-series at various locations on Earth's surface feature clear V-shapes (Fig. 10), that is decadal trends with linear variations that are abruptly interrupted at the times of jerk occurrence. Such V-shapes have been the traditional way to identify geomagnetic jerks. Furthermore, consecutive jerks often show opposite signs, that is alternating V- and inverted V shapes (e.g. Brown *et al.* 2013; Soloviev *et al.* 2017). Our simulated jerk catalogue shows that such sequences are naturally produced by the arrival at the core surface of wave fronts. Whilst the strongest signatures of simulated jerks are most frequently located at low latitudes at the core surface, the effect of the distance from the core surface to observatory locations at Earth's surface, along with the differing sensitivities of the observed field components to the core surface field, results in V-shapes also being obtained at mid to high latitudes in the surface secular variation for the simulated jerks. For instance, simulated jerk events which at the core surface are focused at low latitudes under the Asian hemisphere produce clear signatures on the East component of secular variation in Europe (Figs 10a and d). As is the case for jerks recorded at ground observatories during the 20th century (e.g. Pinheiro *et al.* 2011), the jerk occurrence time measured at the tip of the V-shapes on a given field component can in the simulated jerks show regional delays of a few years with respect to a global occurrence time derived from secular acceleration energy changes. In contrast with the explanation proposed by Pinheiro *et al.* (2011), these delays cannot be ascribed to effects of the finite electrical conductivity of Earth's mantle, which are not included in the 71p model (aside from the impact of a thin basal conducting layer on the global torque balance). The global occurrence time of simulated jerk events is synchronous across the three space components of the field, because these all derive from the same potential. Despite this, delays of a few years can also exist at a specific location between V-shapes measured on different field components (Figs 10 and 11). Systematic analyses of geomagnetic jerks at observatories (see e.g. figs 4 and 5 in Pinheiro *et al.* 2011) also find near-synchronous global occurrence times, but possible local delays across components, both features being also well captured by a potential geomagnetic field model. In our simulation, all these delays simply arise from the geometrical properties of the jerk structure at the core surface, the distance from the core surface to observatory locations and the different geographical sensitivities of the three observed field components to the evolving core surface field.

Consistent with the ground observatory data (Brown *et al.* 2013; Torta *et al.* 2015; Soloviev *et al.* 2017), none of the simulated events can be labelled as completely global with regard to the detectability of jerk V-shapes in the East component, with 'Globality' ratings in Table 2 ranging from about 20–70 per cent of Earth surface. Assessing the detectability of V-shapes in a case where the secular acceleration is not known to the level provided by satellite data, it appears that weaker jerks are difficult to detect (Fig. 12). This may be part of the explanation for the apparent increase of the number of detected jerk events in the past two decades relatively to earlier epochs. In any case, simulated jerks do not necessarily occur on all field components at the same location (Figs 10 and 11), and the East component generally provides the most widespread detection. This suggests that both the geometry of jerk perturbations and a lesser contamination by external fields contribute to the enhanced detectability (e.g. Wardinski & Holme 2011) of geomagnetic jerks on this component.

In summary, the geomagnetic records appear supportive of the existence of routinely recurring deep-triggered wave events. The question of whether these records also support the existence of more extreme, but rarer, near surface-triggered wave events seems to us still open. Prominent characteristics of these events, such as extreme local intensities in the secular variation (Fig. 10d) and significant local reorganization of the core surface magnetic flux (Fig. 5), are difficult to identify in historical records due to the limited geographical coverage at the times of early jerk events. Nonetheless, a detailed reanalysis of the 1969 event, when some satellite observations from the POGO mission are available, may be revealing in this regard. The existence of strong surges in the secular variation intensity (Fig. 13), caused by wave flows temporarily becoming as strong as the background convective flow, is also potentially an important diagnostic for identifying such events. Further study of similar surges, and in particular the one observed in the vicinity of the 1914 geomagnetic jerk (fig. 26 in Jackson & Finlay 2015), seems merited.

Going further backwards in time, it may also be interesting to investigate whether the occurrence of secular variation surges (Fig. 13) during strong, shallow-wave driven simulated jerks may account for events previously labelled as archæomagnetic jerks (see e.g. Gallet *et al.* 2003). From the time resolution standpoint of archæomagnetic studies, the re-organization of Earth's surface magnetic flux over the multidecadal baseline of some events (e.g. events 2 and 9, Fig. 6) may indeed appear as sudden cusps in the field direction amidst more regular secular trends. The typical secular recurrence time of strong simulated jerks (Fig. 1) also appears in line with the observed recurrence of archæomagnetic jerks. We note however that even though they may produce surges in the secular variation at Earth's surface, even the strongest jerks studied here fail to produce sizeable and centennial surges of the field intensity itself, such as those proposed by Gallet *et al.* (2003) for some archæomagnetic jerks. Such variations in field intensity should more naturally point towards mechanisms related to slow convective advection (e.g. Gallet *et al.* 2009), rather than rapid waves.

Because of their strength and proximity to the core surface, near surface triggered wave events are the only events in the present catalogue that provide most insight into the possible signatures of jerks in the time derivative of the length-of-day, caused by accelerations in the magnetic torque exerted on the mantle. The amplitude of the associated inflexions are in line with those observed by Holme & de Viron (2005) and Duan & Huang (2020). These studies argue for a systematic occurrence of this phenomenon at the times of known geomagnetic jerks. While our results support a connection, they underline that the length-of-day signals are frequently weak and difficult to separate from those created by the gravitational torque. We note that end-of-path modelling conditions could make strong length-of-day signatures more common, as the nominal amplitude of the magnetic torque should by multiplied by 7 at these conditions according to the path scaling rules (Aubert *et al.* 2017). Furthermore, the restoring time $I_M/\Gamma\tau = 0.74$ yr responsible for gravitational wiggles in the length of day record is probably too short in the 71p model. With a more realistic upper bound $\Gamma\tau < 10^{21}$ N.m.yr (Pichon *et al.* 2016), this time should be longer than about 70 yr, meaning that interannual inflexions of magnetic origin should stand out much more clearly in the length of day record. It is therefore of interest to clarify the connection between jerks and geodetic signals with further parameter space explorations since the precise

details of the core–mantle coupling mechanisms are important here (Aubert & Finlay 2019).

4.3 Guidelines for future investigations of geomagnetic jerks

With the construction of a catalogue of events from a self-consistent numerical geodynamo simulation, our initial aim was to define geomagnetic jerks in terms of the observed expression of a specific physical process, in order to improve on the essentially phenomenological description that has prevailed so far. The success of simulated jerks produced by hydromagnetic waves in explaining the various features of geomagnetic jerks seen in ground observatory and satellite observations is certainly an encouraging step towards this goal. Our study supports the connection between the arrival of waves at low latitudes at the core surface and pulses in the secular acceleration intensity (Chulliat *et al.* 2010). In this respect, a minimal and dynamically informed definition of geomagnetic jerks should in our opinion focus on the presence of pulses rather than step changes in the secular acceleration. The analysis of our simulated jerk catalogue has shown that apparent step changes in the secular acceleration and all their associated temporal characteristics in fact follow from the hydromagnetic wave dynamics that cause the pulses. This alleviates earlier concerns regarding the theoretically ill-posed character of a step change, which would formally correspond to a flat and non-converging frequency spectrum of geomagnetic acceleration (Bouligand *et al.* 2016, AG21).

This change of perspective should naturally motivate further work targeted at improving our knowledge of the dynamic (secular acceleration, flow acceleration) rather than kinematic (secular variation, flow patterns) aspects of geomagnetic observables. A marker of the connection between jerks and hydromagnetic waves is the temporary dominance of flow acceleration in the budget of magnetic acceleration (Fig. 2). More specifically, the flow acceleration patterns to look for are non-axisymmetric, low-latitude and equatorially symmetric, rapidly alternating interannual components with short latitudinal, but long longitudinal length scales which facilitate their detection as quasi-geostrophic, magneto-Coriolis waves (Fig. 9 and Gillet *et al.* 2022b). Because signatures of QGMC waves at the Earth's core surface (Gillet *et al.* 2022b), and also in the simulations (AG21) are apparently rather common, geomagnetic jerks should be seen as particularly prominent, and easily observed, parts of a dynamic continuum that involves a constant excitation of hydromagnetic waves in the system. The simulated events furthermore support the idea that successive prominent jerks can be a collective result of a single wave packet. A better characterization of the involved waves is important because they carry information on the medium through which they pass, thereby providing a possibility of magnetic sounding of the core interior. This information is necessary if we are to achieve more reliable future predictions of the geomagnetic field evolution. One outstanding difficulty here is the need for a better spatio-temporal resolution in the retrieval of magnetic variations and their associated core flows, since small, currently unresolved scales, make important contributions to the diagnostic W/C (Table 2, Fig. 2). In this respect, new field modelling techniques, such as those based on local averaging rather than global analyses (e.g. Hammer & Finlay 2019; Hammer *et al.* 2021) may allow an improved spatial and temporal resolution for the secular acceleration, for example at low latitudes. Improved techniques for solving the core surface flow inverse problem utilizing prior information from numerical simulations (e.g. Gillet *et al.* 2019) are also needed in the quest to probe the peculiar hydromagnetic wave structures producing jerks.

Global and sustained satellite magnetic measurements have been key to improving the reliability of geomagnetic acceleration models. The present 20-yr-long record is not yet sufficiently long to encompass the rich variety of dynamic features suggested by the simulated jerk catalogue. This provides a powerful scientific justification for maintaining low Earth orbiting, dedicated geomagnetic satellites (see Hulot *et al.* 2018). In particular, the question of whether the geodynamo can support more dramatic jerk events, resulting from waves triggered near to the core surface, is still open. This point has important geodynamic implications, because the existence of such jerks would help to constrain the buoyancy distribution at the core surface, with stable stratification presumably precluding the shallow plumes that underlie such events. To investigate this question, and because of the prominent expected signatures of such jerks in the intensity of the secular variation, re-analyses of past ground observatory records (especially at low latitudes) may also be a fruitful avenue for future observational research.

ACKNOWLEDGMENTS

The authors wish to thank William Brown and an anonymous referee for comments that helped to improve the manuscript, and Dominique Jault for discussions. JA acknowledges support from the Fondation Simone et Cino Del Duca of Institut de France (2017 Research Grant). This project has also been funded by ESA in the framework of EO Science for Society, through contract 4000127193/19/NL/IA (SWARM + 4D Deep Earth: Core). NG has been partially supported by the French Centre National d'Etudes Spatiales (CNES) for the study of Earth's core dynamics in the context of the Swarm mission of ESA. Numerical computations were performed at S-CAPAD, IPGP and using HPC resources from GENCI-TGCC and, GENCI-IDRIS and GENCI-CINES (Grant numbers A0080402122, A0100402122 and A0120402122). The results presented in this work rely on data collected at magnetic observatories. The authors thank the national institutes that support them and INTERMAGNET for promoting high standards of magnetic observatory practice (www.intermagnet.org).

DATA AVAILABILITY

The numerical code and simulation data analysed in this study are available from the corresponding author upon reasonable request. Data and additional video files from the numerical model are also available online at the URLs https://4d-earth-swarm.univ-grenoble-alpes.fr/datahttps://www.ipgp.fr/~aubert/4dearth

REFERENCES

Ahrens, T.J., 1995. *Global Earth Physics: A Handbook of Physical Constants,* Vol. **1,** AGU.

Alexandrescu, M., Gibert, D., Hulot, G., Le Mouël, J.-L. & Saracco, G., 1996. Worldwide wavelet analysis of geomagnetic jerks, *J. geophys. Res.,* **101**(B10), 21 975–21 994.

Aubert, J., 2015. Geomagnetic forecasts driven by thermal wind dynamics in the Earth's core, *Geophys. J. Int.,* **203**(3), 1738–1751.

Aubert, J., 2018. Geomagnetic acceleration and rapid hydromagnetic wave dynamics in advanced numerical simulations of the geodynamo, *Geophys. J. Int.,* **214**(1), 531–547.

Aubert, J., 2019. Approaching Earth's core conditions in high-resolution geodynamo simulations, *Geophys. J. Int.,* **219**(S1), S137–S151.

Aubert, J., 2020. Recent geomagnetic variations and the force balance in Earth's core, *Geophys. J. Int.,* **221**(1), 378–393.

Aubert, J. & Dumberry, M., 2011. Steady and fluctuating inner core rotation in numerical geodynamo models, *Geophys. J. Int.,* **184**(1), 162–170.

Aubert, J. & Finlay, C.C., 2019. Geomagnetic jerks and rapid hydromagnetic waves focusing at Earth's core surface, *Nat. Geosci.,* **12**(5), 393–398.

Aubert, J. & Gillet, N., 2021. The interplay of fast waves and slow convection in geodynamo simulations nearing Earth's core conditions, *Geophys. J. Int.,* **225,** 1854–1873.

Aubert, J., Finlay, C.C. & Fournier, A., 2013. Bottom-up control of geomagnetic secular variation by the Earth's inner core, *Nature,* **502,** 219–223.

Aubert, J., Gastine, T. & Fournier, A., 2017. Spherical convective dynamos in the rapidly rotating asymptotic regime, *J. Fluid. Mech.,* **813,** 558–593.

Bärenzung, J., Holschneider, M., Wicht, J., Sanchez, S. & Lesur, V., 2018. Modeling and predicting the short-term evolution of the geomagnetic field, *J. geophys. Res.,* **123**(6), 4539–4560.

Bloxham, J., Zatman, S. & Dumberry, M., 2002. The origin of geomagnetic jerks, *Nature,* **420**(6911), 65–68.

Bouligand, C., Gillet, N., Jault, D., Schaeffer, N., Fournier, A. & Aubert, J., 2016. Frequency spectrum of the geomagnetic field harmonic coefficients from dynamo simulations, *Geophys. J. Int.,* **207**(2), 1142–1157.

Brown, W., Mound, J. & Livermore, P., 2013. Jerks abound: An analysis of geomagnetic observatory data from 1957 to 2008, *Phys. Earth planet. Inter.,* **223,** 62–76.

Chi-Durán, R., Avery, M.S., Knezek, N. & Buffett, B.A., 2020. Decomposition of geomagnetic secular acceleration into traveling waves using complex empirical orthogonal functions, *Geophys. Res. Lett.,* **47**(17), e2020GL087940 , doi:10.1029/2020GL087940.

Christensen, U.R., Aubert, J. & Hulot, G., 2010. Conditions for Earth-like geodynamo models, *Earth planet. Sci. Lett.,* **296**(3–4), 487–496.

Chulliat, A. & Maus, S., 2014. Geomagnetic secular acceleration, jerks, and a localized standing wave at the core surface from 2000 to 2010, *J. Geophys. Res.,* **119**(3), 1531–1543.

Chulliat, A., Thebault, E. & Hulot, G., 2010. Core field acceleration pulse as a common cause of the 2003 and 2007 geomagnetic jerks, *Geophys. Res. Lett.,* **37**(7), doi:10.1029/2009GL042019.

Chulliat, A., Alken, P. & Maus, S., 2015. Fast equatorial waves propagating at the top of the Earth's core, *Geophys. Res. Lett.,* **42**(9), 3321–3329.

Courtillot, V., Ducruix, J. & Le Mouël, J.-L., 1978. Sur une accélération récente de la variation séculaire du champ magnétique terrestre, *C.R. Acad. Sci. Paris. D,* **287**(12), 1095–1098.

Davies, C., Pozzo, M., Gubbins, D. & Alfè, D., 2015. Constraints from material properties on the dynamics and evolution of earth's core, *Nat. Geosci.,* **8**(9), 678–685.

De Michelis, P., Cafarella, L. & Meloni, A., 1998. Worldwide character of the 1991 geomagnetic jerk, *Geophys. Res. Lett.,* **25**(3), 377–380.

Duan, P. & Huang, C., 2020. Intradecadal variations in length of day and their correspondence with geomagnetic jerks, *Nat. Commun.,* **11,** doi:10.1038/s41467-020-16109-8.

Finlay, C.C., Olsen, N., Kotsiaros, S., Gillet, N. & Tøffner-Clausen, L., 2016. Recent geomagnetic secular variation from Swarm and ground observatories as estimated in the CHAOS-6 geomagnetic field model, *Earth, Planets Space,* **68,** doi:10.1186/s40623-016-0486-1.

Finlay, C.C., Kloss, C., Olsen, N., Hammer, M.D., Tøffner-Clausen, L., Grayver, A. & Kuvshinov, A., 2020. The CHAOS-7 geomagnetic field model and observed changes in the South Atlantic Anomaly, *Earth Planets Space,* **72**(1), 156.

Frost, D.A. *et al.*, 2022. Multidisciplinary constraints on the thermal-chemical boundary between earth's core and mantle, *Geochem. Geophys. Geosyst.,* **23**(3), e2021GC009764.

Gallet, Y., Genevey, A. & Courtillot, V., 2003. On the possible occurrence of 'archaeomagnetic jerks' in the geomagnetic field over the past three millennia, *Earth planet. Sci. Lett.,* **214**(1), 237–242.

Gallet, Y., Hulot, G., Chulliat, A. & Genevey, A., 2009. Geomagnetic field hemispheric asymmetry and archeomagnetic jerks, *Earth planet. Sci. Lett.,* **284**(1), 179–186.

Gerick, F., Jault, D. & Noir, J., 2021. Fast quasi-geostrophic Magneto-Coriolis modes in the Earth's core, *Geophys. Res. Lett.,* **48**(4), e2020GL090803.

Gillet, N., Jault, D. & Finlay, C.C., 2015. Planetary gyre, time-dependent eddies, torsional waves and equatorial jets at the Earth's core surface, *J. geophys. Res.,* **120,** 3991–4013.

Gillet, N., Huder, L. & Aubert, J., 2019. A reduced stochastic model of core surface dynamics based on geodynamo simulations, *Geophys. J. Int.,* **219**(1), 522–539.

Gillet, N., Gerick, F., Angappan, R. & Jault, D., 2022a. A dynamical prospective on interannual geomagnetic field changes, *Surv. Geophys.,* **43**(1), 71–105.

Gillet, N., Gerick, F., Jault, D., Schwaiger, T., Aubert, J. & Istas, M., 2022b. Satellite magnetic data reveal interannual waves in Earth's core, *PNAS,* **119**(13), e2115258119.

Gillet, N., Jault, D., Canet, E. & Fournier, A., 2010. Fast torsional waves and strong magnetic field within the Earth's core, *Nature,* **465**(7294), 74–77.

Gubbins, D. & Roberts, N., 1983. Use of the frozen flux approximation in the interpretation of archaeomagnetic and palaeomagnetic data, *Geophys. J. Int.,* **73**(3), 675–687.

Hammer, M.D. & Finlay, C.C., 2019. Local averages of the core–mantle boundary magnetic field from satellite observations, *Geophys. J. Int.,* **216**(3), 1901–1918.

Hammer, M.D., Finlay, C.C. & Olsen, N., 2021. Applications for CryoSat-2 satellite magnetic data in studies of earth's core field variations, *Earth Planets Space,* **73,** doi:10.1186/s40623-021-01365-9.

Hide, R., 1966. Free hydromagnetic oscillations of the earth's core and the theory of the geomagnetic secular variation, *Phil. Trans. R. Soc. A,* **259**(1107), 615–647.

Holme, R. & de Viron, O., 2005. Geomagnetic jerks and a high-resolution length-of-day profile for core studies, *Geophys. J. Int.,* **160**(2), 435–439.

Holme, R. & de Viron, O., 2013. Characterization and implications of intradecadal variations in length of day, *Nature,* **499**(7457), 202–204.

Hulot, G. *et al.*, 2018. Nanosatellite high-precision magnetic missions enabled by advances in a stand-alone scalar/vector absolute magnetometer, in *IGARSS 2018: 2018 IEEE International Geoscience and Remote Sensing Symposium: Observing, Understanding and Forecasting The Dynamics of Our Planet,* 22–27 July 2018, Valencia, Spain, pp. 6320–6323, IEEE.

Jackson, A. & Finlay, C., 2015. Geomagnetic secular variation and its applications to the core, in *Treatise on Geophysics,* 2nd edn, pp. 137–184, ed. Schubert, G., Elsevier.

Jackson, A., Bloxham, J. & Gubbins, D., 1993. Time-dependent flow at the core surface and conservation of angular momentum in the coupled core-mantle system, in *Dynamics of the Earth's Deep Interior and Earth Rotation,* Vol. **72,** pp. 97–107, eds Le Mouël, J.-L., Smylie, D.E. & Herring, T., AGU Geophysical Monograph.

Jault, D., Gire, C. & Le Mouël, J.-L., 1988. Westward drift, core motions and exchanges of angular momentum between core and mantle, *Nature,* **333,** 353–356.

Kloss, C. & Finlay, C.C., 2019. Time-dependent low-latitude core flow and geomagnetic field acceleration pulses, *Geophys. J. Int.,* **217**(1), 140–168.

Konôpková, Z., McWilliams, R.S., Gómez-Pérez, N. & Goncharov, A.F., 2016. Direct measurement of thermal conductivity in solid iron at planetary core conditions, *Nature,* **534**(7605), 99–101.

Le Huy, M., Alexandrescu, M., Hulot, G. & Le Mouël, J.-L., 1998. On the characteristics of successive geomagnetic jerks, *Earth Planets Space,* **50**(9), 723–732.

Le Mouël, J.-L., Ducruix, J. & Ha Duyen, C., 1982. The worldwide character of the 1969–1970 impulse of the secular acceleration rate, *Phys. Earth planet. Inter.,* **28**(4), 337–350.

Lehnert, B., 1954. Magnetohydrodynamic waves under the action of the coriolis force, *Astrophys. J.,* **119,** 647, doi:10.1086/145869.

Lesur, V., Gillet, N., Hammer, M.D. & Mandea, M., 2022. Rapid variations of Earth's core magnetic field, *Surv. Geophys.,* **43**(1), 41–69.

Lesur, V., Wardinski, I., Hamoudi, M. & Rother, M., 2010. The second generation of the GFZ reference internal magnetic model: GRIMM-2, *Earth Planets Space,* **62**(10), 765–773.

Livermore, P.W., Fournier, A., Gallet, Y. & Bodin, T., 2018. Transdimensional inference of archeomagnetic intensity change, *Geophys. J. Int.,* **215**(3), 2008–2034.

Malin, S. R.C. & Hodder, B.M., 1982. Was the 1970 geomagnetic jerk of internal or external origin?, *Nature,* **296**(5859), 726–728.

Malin, S.R.C., Hodder, B.M. & Barraclough, D.R., 1983. Geomagnetic secular variation: a jerk in 1970, in *Scientific Contributions in Commemoration of Ebro Observatory's 75th Anniversary*.

Mandea, M., Holme, R., Pais, A., Pinheiro, K., Jackson, A. & Verbanac, G., 2010. Geomagnetic jerks: rapid core field variations and core dynamics, *Space. Sci. Rev.,* **155**(1), 147–175.

Pichon, G., Aubert, J. & Fournier, A., 2016. Coupled dynamics of Earth's geomagnetic westward drift and inner core super-rotation, *Earth planet. Sci. Lett.,* **437,** 114–126.

Pinheiro, K.J., Jackson, A. & Finlay, C.C., 2011. Measurements and uncertainties of the occurrence time of the 1969, 1978, 1991, and 1999 geomagnetic jerks, *Geochem. Geophys. Geosyst.,* **12**(10), doi:10.1029/2011GC003706.

Pozzo, M., Davies, C.J., Gubbins, D. & Alfè, D., 2012. Thermal and electrical conductivity of iron at Earth's core conditions, *Nature,* **485**(7398), 355–358.

Sambridge, M., Gallagher, K., Jackson, A. & Rickwood, P., 2006. Transdimensional inverse problems, model comparison and the evidence, *Geophys. J. Int.,* **167**(2), 528–542.

Schaeffer, N., 2013. Efficient spherical harmonic transforms aimed at pseudospectral numerical simulations, *Geophys. Geochem. Geosyst.,* **14**(3), 751–758.

Schwaiger, T., Gastine, T. & Aubert, J., 2019. Force balance in numerical geodynamo simulations: a systematic study, *Geophys. J. Int.,* **219**(S1), S101–S114.

Silva, L. & Hulot, G., 2012. Investigating the 2003 geomagnetic jerk by simultaneous inversion of the secular variation and acceleration for both the core flow and its acceleration, *Phys. Earth planet. Inter.,* **198–199,** 28–50.

Soloviev, A., Chulliat, A. & Bogoutdinov, S., 2017. Detection of secular acceleration pulses from magnetic observatory data, *Phys. Earth. planet. Inter.,* **270,** 128–142.

Torta, J.M., Pavón-Carrasco, F.J., Marsal, S. & Finlay, C.C., 2015. Evidence for a new geomagnetic jerk in 2014, *Geophys. Res. Lett.,* **42**(19), 7933–7940.

Wardinski, I. & Holme, R., 2011. Signal from noise in geomagnetic field modelling: denoising data for secular variation studies, *Geophys. J. Int.,* **185**(2), 653–662.

Wardinski, I., Holme, R., Asari, S. & Mandea, M., 2008. The 2003 geomagnetic jerk and its relation to the core surface flows, *Earth planet. Sci. Lett.,* **267**(3–4), 468–481.

Zatman, S. & Bloxham, J., 1997. Torsional oscillations and the magnetic field within the Earth's core, *Nature,* **388,** 760–763.